Agenzia nazionale per le nuove tecnologie, l'energia
e lo sviluppo economico sostenibile

Ministero dello Sviluppo Economico

RICERCA DI SISTEMA ELETTRICO

Contributo a EERA su caratterizzazione materiali mediante diffusione e diffrazione neutronica

Roberto Coppola

RdS/2012/145

CONTRIBUTO A EERA SU CARATTERIZZAZIONE MATERIALI MEDIANTE DIFFUSIONE E DIFFRAZIONE NEUTRONICA

*Roberto Coppola E*NEA

Settembre 2012

Report Ricerca di Sistema Elettrico
Accordo di Programma Ministero dello Sviluppo Economico - ENEA
Area: Governo, Gestione e Sviluppo**,** del Sistema Elettrico Nazionale
Progetto: Nuovo Nucleare da Fissione: Collaborazioni Internazionali e sviluppo Competenze in Materia Nucleare
Responsabile del Progetto: Massimo Sepielli,ENEA

ENEA Ricerca Sistema Elettrico	Sigla di identificazione	Distrib.	Pag. di
	PAR2011-ENEA-L1C1- 018	L	1 20

Titolo

Contributo a EERA su caratterizzazione materiali mediante diffusione netronica ai piccoli angoli e diffrazione neutronica

Descrittori

Tipologia del documento: Rapporto Tecnico

Collocazione contrattuale: ACCORDO DI PROGRAMMA Ministero dello Sviluppo Economico – ENEA sulla Ricerca di Sistema Elettrico PIANO ANNUALE DI REALIZZAZIONE 2011 Progetto 1.3.1: Energia nucleare: NUOVO NUCLEARE DA FISSIONE: COLLABORAZIONI INTERNAZIONALI E SVILUPPO COMPETENZE IN MATERIA NUCLEARE, PAR 2011.

Argomenti trattati:

Sommario

L'attività ha consistito in una serie di prove di diffusione neutronica ai piccoli angoli e diffrazione neutronica eseguite presso il Reattore ad Alto Flusso dell'Institut Max von Laue – Paul Langevin (ILL) di Grenoble, Francia, su materiali di interesse per il nucleare da fissione, in particolare nell'ambito del Progetto EERA JPNM (European Energy Research Alliance Joint Programme on Nuclear Materials) e di due Progetti Coordinati di Ricerca dell'IAEA (International Atomic Energy Agency). Sono stati prevalentemente studiati acciai strutturali a rinforzo ceramico o "ODS" (*oxide dispersion strengthened*), che vengono attualmente considerati una delle soluzioni più promettenti per i futuri reattori di IV generazione ma che richiedono ancora una messa a punto dei processi di produzione e della caratterizzazione meccanica e microstrutturale. Su diversi tipi di tali acciai "ODS", sia ferritico/martensitici sia austenitici, sono state eseguite misure di diffusione neutronica ai piccoli angoli per caratterizzare la presenza di difetti microstrutturali (precipitati, nano-particelle ceramiche) e misure di diffrazione neutronica per identificare le fasi cristallografiche nei vari tipi di materiale. I risultati ottenuti hanno fornito significative informazioni sulla stabilità microstrutturale nel corso di trattamenti termici fino ad elevate temperature e hanno consentito di rivelare fasi minoritarie, non sempre corrispondenti a quelle nominalmente presenti, di cui occorrerà tenere conto nella messa a punto dei processi di produzione. L'insieme di queste ricerche ha prodotto inoltre una metodologia sperimentale di interesse generale per la caratterizzazione dei materiali nucleari e ha consentito all'ENEA di accedere a programmi internazionali, quali EERA JPNM.

Note

Copia n.			In carico a:			
2			NOME			
			FIRMA			
1			NOME			
			FIRMA			
0	EMISSIONE	21.09.12	NOME	R.Coppola	M.Sepielli	M.Sepielli
			FIRMA			
REV.	DESCRIZIONE	DATA		REDAZIONE	CONVALIDA	APPROVAZIONE

Sommario

Sommario

L'attività ha consistito in una serie di prove di diffusione neutronica ai piccoli angoli e diffrazione neutronica eseguite presso il Reattore ad Alto Flusso dell'Institut Max von Laue – Paul Langevin (ILL) di Grenoble, Francia, su materiali di interesse per il nucleare da fissione, in particolare nell'ambito del Progetto EERA JPNM (European Energy Research Alliance Joint Programme on Nuclear Materials) e di due Progetti Coordinati di Ricerca dell'IAEA (International Atomic Energy Agency). Sono stati prevalentemente studiati acciai strutturali a rinforzo ceramico o "ODS" (*oxide dispersion strengthened*), che vengono attualmente considerati una delle soluzioni più promettenti per i futuri reattori di IV generazione ma che richiedono ancora una messa a punto dei processi di produzione e della caratterizzazione meccanica e microstrutturale. Su diversi tipi di tali acciai "ODS", sia ferritico/martensitici sia austenitici, sono state eseguite misure di diffusione neutronica ai piccoli angoli per caratterizzare la presenza di difetti microstrutturali (precipitati, nano-particelle ceramiche) e misure di diffrazione neutronica per identificare le fasi cristallografiche nei vari tipi di materiale. I risultati ottenuti hanno fornito significative informazioni sulla stabilità microstrutturale nel corso di trattamenti termici fino ad elevate temperature e hanno consentito di rivelare fasi minoritarie, non sempre corrispondenti a quelle nominalmente presenti, di cui occorrerà tenere conto nella messa a punto dei processi di produzione. L'insieme di queste ricerche ha prodotto inoltre una metodologia sperimentale di interesse generale per la caratterizzazione dei materiali nucleari e ha consentito all'ENEA di accedere a programmi internazionali, quali EERA JPNM.

Summary

This activity consisted in a series of small-angle neutron scattering and diffraction measurements carried out at the High Flux Reactor of the Institut Max von Laue – Paul Langevin (ILL) in Grenoble, France, on fission relevant materials, namely in the frame of the EERA JPNM Project (European Energy Research Alliance Joint Programme on Nuclear Materials) and of two Coordinated Research Projects of the IAEA (International Atomic Energy Agency). Oxide dispersion strengthened ("ODS") structural steels have been mainly

investigated, since these materials are currently considered as one of the most promising options for Gen IV reactors, although they still require developments in fabrication routes and characterization, both mechanical and microstructural. Different types of such ODS steels, both ferritic/martenisitic and austenic, have been investigated by small-angle neutron scattering to characterize microstructural defects (precipitates, ceramic nano particles) and by neutron diffraction to identify the crystallographic phases present in the different materials and following different treatments. The obtained results have provided relevant information on microstructural stability under high-temperature treatments and allowed to detect minority phases, not always corresponding to the nominally present ones, to be taken into account for the development of fabrication routes. This research programme, furthermore, resulted in an experimental procedure of general interest to nuclear materials and favoured the participation of the ENEA to international programmes such as EERA JPNM.

Introduzione

L'attività ha consistito in una serie di prove di diffusione e diffrazione neutronica eseguite presso il Reattore ad Alto Flusso dell'Institut Max von Laue – Paul Langevin (ILL) di Grenoble, Francia, su materiali di interesse per il nucleare da fissione, al quale l'ENEA fa regolarmente ricorso da tempo per ricerche nell'ambito delle proprie attività programmatiche sui materiali per il settore energetico (fissione, fusione, celle a combustibile). Tale attività è stata innanzitutto finalizzata alla messa a punto di metodologie sperimentali e all'acquisizione di risultati tecnico-scientifici rilevanti per una partecipazione dell'ENEA alla fase preparatoria del Progetto EERA JPNM (European Energy Research Alliance Joint Programme on Nuclear Materials) e successivamente per l'acquisizione dei relativi finanziamenti europei in collaborazione con altri Laboratori. Tali attività si sono inoltre svolte nell'ambito dei seguenti due Progetti Coordinati di Ricerca (CRP, Coordinated Research Project) dell'IAEA (International Atomic Energy Agency) ai quali pure partecipa l'ENEA:

IAEA CRP 1575 – *Development, Characterization and Testing of Materials of Relevance to Nuclear Energy Sector Using Neutron Beams*

IAEA CRP 11006 - *Benchmarking of Structural Materials Pre-selected for Advanced Nuclear Reactors*.

Lo scopo principale di tali CRP è promuovere e coordinare la collaborazione internazionale relativamente all'utilizzo delle tecniche neutroniche per la qualifica dei materiali nucleari, favorendo scambio di conoscenze e risultati tra i partecipanti e coordinando l'accesso alle sorgenti neutroniche intense in modo da ottimizzarne l'utilizzo.

In tale contesto, sono stati prevalentemente studiati acciai strutturali a rinforzo ceramico o "ODS" (*oxide dispersion strengthened*), che vengono attualmente considerati una delle soluzioni più promettenti per i futuri reattori di IV generazione ma che richiedono ancora una messa a punto dei processi di produzione e della caratterizzazione meccanica e

microstrutturale. Su diversi tipi di tali acciai “ODS”, sia ferritico/martensitici sia austenitici, sono state eseguite misure di diffusione neutronica ai piccoli angoli per caratterizzare la presenza di difetti microstrutturali (precipitati, nano-particelle ceramiche) e misure di diffrazione neutronica per identificare le fasi cristallografiche nei vari tipi di materiale. I materiali studiati sono stati forniti dal Karlsruhe Institut of Technology (KIT), con il quale l’ENEA collabora sia in ambito EERA sia in ambito IAEA, e dall’Università di Pechino (nostro partner IAEA). Dopo aver introdotto le tecniche sperimentali utilizzate e i materiali studiati, vengono presentati i risultati ottenuti, discutendo l’apporto di queste ricerche al miglioramento degli acciai ODS e gli auspicabili sviluppi di tali attività sperimentali; vengono infine allegate le pubblicazioni scientifiche conseguite.

Metodologia sperimentale utilizzata

Le tecniche di diffusione e diffrazione neutronica si basano sull’utilizzo di fasci collimati di neutroni di bassa energia (< 25 meV), estratti da reattori di ricerca appositamente costruiti e dotati preferenzialmente di una sorgente “fredda” (H liquido) all’interno del nocciolo per ottenere le caratteristiche spettrali necessarie a questo tipo di misure; i rif. (1,2) presentano una introduzione e una descrizione di tali tecniche, che possono essere sia anelastiche (con scambio di energia tra fascio neutronico e campione studiato) sia anelastiche (senza scambio di energia) come quelle utilizzate nel presente studio per studiare proprietà conformazionali e cristallografiche dei materiali in esame. L’utilizzo delle tecniche neutroniche, complementari a quelle basate sull’utilizzo dei raggi X, presenta i seguenti vantaggi:

- il coefficiente di assorbimento dei neutroni di bassa energia consente lo studio non-distruttivo di campioni massivi

- l’interazione dei neutroni con i singoli elementi della tabella periodica non varia proporzionalmente al numero atomico, come nel caso dei raggi X, ma casualmente dall’uno all’altro, di conseguenza importanti costituenti dei materiali nucleari, come Fe e Cr, non distinguibili con i raggi X, sono ben distinti dai fasci neutronici

- il neutrone è dotato di un momento magnetico di *spin*, che rappresenta una insostituibile sonda del magnetismo della materia condensata.

Le due tecniche utilizzate sono la diffusione neutronica ai piccoli angoli (*small-angle neutron scattering: SANS*) e la diffrazione neutronica. La **diffusione neutronica ai piccoli angoli** si basa sull'allargamento entro un intervallo angolare $\theta < 5°$ di un fascio neutronico collimato, di lunghezza d'onda λ, quando passi attraverso un campione contenente difetti microstrutturali quali precipitati o microvuoti; la fig. 1 illustra il principio di tale tecnica e mostra una foto dello strumento D22, installato presso l'ILL (3), sul quale sono state eseguite le misure qui di seguito riportate. Nel caso di materiali magnetici, quali gli acciai ferritico/martensitici studiati, occorre eseguire le misure in presenza di un campo magnetico intenso (1 T) che saturi la magnetizzazione all'interno del campione consentendo di distinguere le sezioni d'urto neutroniche magnetica e nucleare, come riportato nella fig. 2.

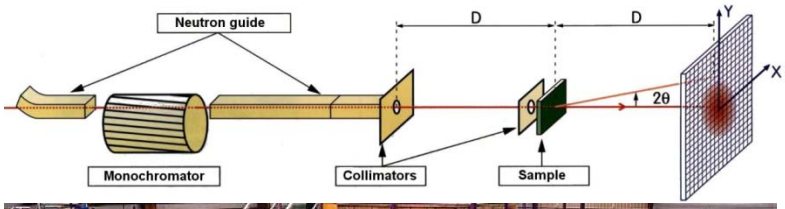

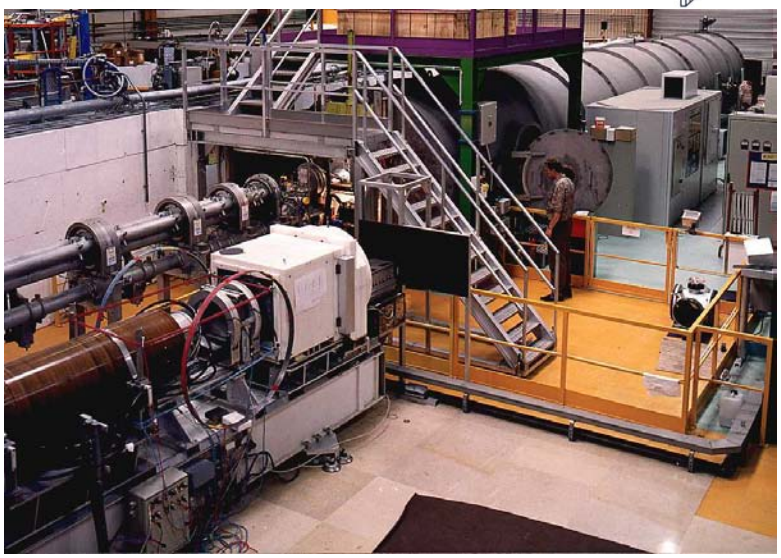

Fig. 1 – Schema della tecnica di diffusione neutronica ai piccoli angoli e foto dello strumento D22 presso l'ILL-Grenoble

Per ciascuna di queste due componenti, nucleare e magnetica, dopo opportune calibrazioni, si misura una sezione d'urto che nel caso di sistemi polidispersi a bassa frazione volumica, quali quelli studiati, è così definita:

$$\frac{d\Sigma(Q)}{d\Omega} = (\Delta\rho)^2 \int_0^\infty dR\, N(R) V^2(R) \left|F(Q,R)\right|^2 \qquad (1)$$

dove $Q = 4\pi \sin\theta/\lambda$, $(\Delta\rho)^2$ è il "contrasto" tra matrice e microdifetti (differenza in densità di lunghezza di diffusione coerente), F il fattore di forma dei microdifetti (sferico, nel caso dei materiali studiati), R il raggio di tali difetti, V il loro volume e $N(R)$ la loro distribuzione dimensionale, che va determinata con trasformazione inversa di tale equazione; tale operazione si può effettuare tramite diversi codici di calcolo, tra cui quello messo a punto da tempo dall'ENEA e discusso nel rif. (4). La combinazione delle due sezioni d'urto, magnetica e nucleare, attraverso il seguente rapporto:

$$R(Q) = \frac{\frac{d\Sigma(Q)}{d\Omega_{nucl}} + \frac{d\Sigma(Q)}{d\Omega_{mag}}}{\frac{d\Sigma(Q)}{d\Omega_{nucl}}} = 1 + (\Delta\rho)^2_{mag} / (\Delta\rho)^2_{nucl} \qquad (2)$$

consente di misurare il rapporto tra "contrasto" nucleare e magnetico dei micro difetti e quindi di ottenere ulteriori informazioni sulla loro natura.

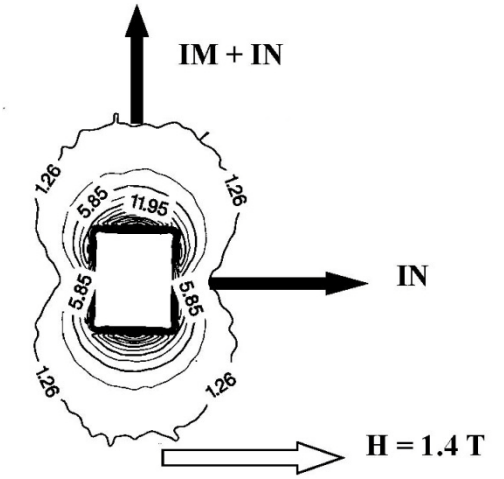

Fig. 2 – Tipico spettro bi-dimensionale di diffusione neutronica ai piccoli angoli, con relative linee di isointensità, di un campione magnetico; H è il campo magnetico esterno

La **diffrazione neutronica** si basa sulla ben nota legge di Bragg

$$\lambda = 2d \,\text{sen}\theta \qquad (3)$$

che collega la maglia cristallografica d con l'angolo θ sotto il quale si osserva il corrispondente picco di diffrazione data un lunghezza d'onda λ della radiazione incidente. Le misure sono state effettuate presso il diffrattometro D20 dell'ILL (5), che viene mostrato in fig. 3, utilizzando una lunghezza d'onda λ=0.136 nm, che ha consentito di esplorare tutto l'intervallo angolare necessario a rivelare le varie fasi presenti. L'analisi dei dati è stata eseguita mediante il codice FULLPROF (6), che consiste in un *best-fit* tra dati sperimentali e possibili fasi presenti (corrispondenti a ben definiti picchi di diffrazione).

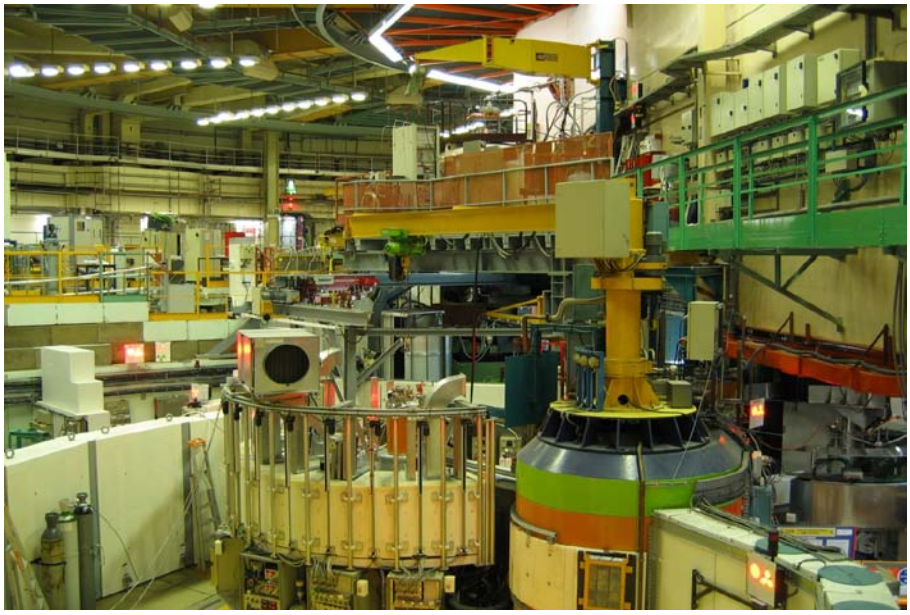

Fig. 3 – Foto del diffrattometro per diffrazione neutronica ad alta risoluzione D20 presso l'ILL-Grenoble

Materiali studiati

Gli acciai ODS studiati sono stati selezionati tra i materiali più promettenti e meglio conosciuti in ambito internazionale, in particolare in riferimento allo sviluppo del progetto EERA e alle attività dei gruppi di lavoro IAEA sopra citati. Una prima serie di acciai ODS, ferritico/martensitici, è stata fornita dal KIT, che è uno dei principali laboratori europei impegnato nella produzione pre-industriale di significative quantità di tali materiali e relativi manufatti (7). Il KIT produce sia in forma policristallina sia come nanopolveri ottenute da alligazione meccanica, acciai ferritico/martensitici con contenuti di Cr tra il 9 e il 14 wt% e di fase ceramica Y_2O_3 dello 0,3 o dello 0,5 wt %. E' inoltre in corso uno studio sistematico dell'effetto di aggiunte di W (1–2 wt%) e di Ti (0.1–0.2 wt%) sulla stabilità e sulla resistenza dei vari tipi di acciai cosi ottenuti, sui quali vengono eseguite prove termo meccaniche e

caratterizzazioni microstrutturali per studiare la dimesione dei grani e le distribuzioni dimensionali della fasi di precipitati prodotti. In tale contesto, l'ENEA aveva già in passato eseguito misure di diffusione neutronica ai piccoli angoli su alcuni di questi materiali, ottenendo distribuzioni dimensionali della fase Y_2O_3 in ottimo accordo con risultati di microscopia elettronica (8) e una prima serie di informazioni microstrutturali sull'evoluzione dei precipitati in nano polveri sottoposte a rinvenimento tra 700°C e 1150°C (9).

La seconda serie di acciai ODS studiata, fornita dall'Università di Pechino, comprende una serie di campioni di acciaio austenitico ODS 18 Cr 0.35 Y_2O_3 wt% ottenuti tramite una combinazione di alligazione meccanica e pressatura isostatica a caldo (10) e già in parte caratterizzati con misure di diffrazione X e tecniche di microscopia elettronica; per confronto, l'Università di Pechino ha anche fornito acciai ferritico/martensitici 9 Cr 0.35 Y_2O_3 wt% prodotti con identica metodologia.

Risultati ottenuti

Tra i più significativi risultati ottenuti sugli acciai di provenienza KIT, la fig. 4 mostra la differenza tra le sezioni d'urto di diffusione neutronica ai piccoli angoli dell'acciaio ferritico/martensitico 9 Cr 0.35 Y_2O_3 wt% prima e dopo aggiunta di Ti 0.4 wt%: ad alti valori di Q (corrispondenti a dimensioni dei precipitati di pochi nm) la presenza del Ti nella lega produce un notevole aumento della sezione d'urto, che viene interpretato come la formazione di una nuova fase di precipitati. Questa è visibile nella fig. 5, che riporta le distribuzioni dimensionali relative alle due curve della fig. 4, mostrando la nuova popolazione di micro difetti (precipitati del tipo TiN) in presenza di Ti. La fig. 5 mostra l'andamento del rapporto *R(Q)* per i due campioni studiati: il materiale di partenza, privo di Ti, ha un andamento complesso di *R(Q)*, indice della presenza di fasi con diversa composizione chimica, mentre l'aggiunta di Ti produce un *R(Q)* pressoché costante su tutto l'intervallo sperimentale considerato, indice di una maggiore omogeneità chimica dei difetti microstruturali. Sono in corso verifiche e calcoli, basati anche su informazioni metallurgiche e di microscopia analitica, per completare l'interpretazione di tali risultati identificando con precisione la natura delle fasi osservate.

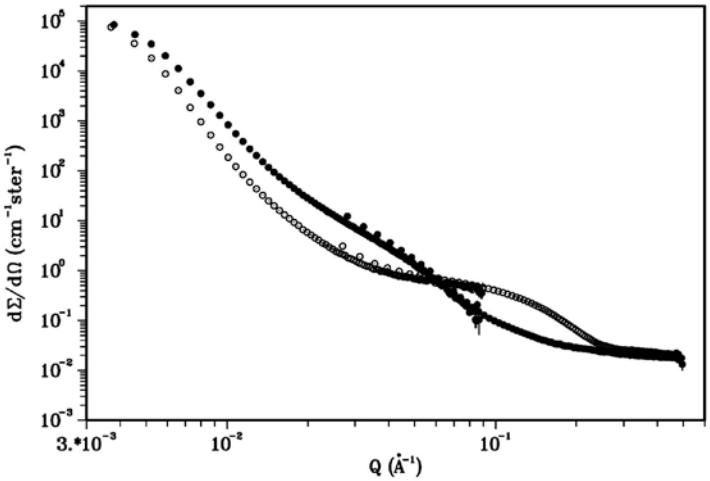

Fig. 4 - Sezioni d'urto di diffusione neutronica ai piccoli angoli (componente nucleare) dell'acciaio ferritico/martensitico 9 Cr 0.35 Y_2O_3 wt% prima (cerchi pieni) e dopo (cerchi vuoti) aggiunta di Ti 0.4 wt%.

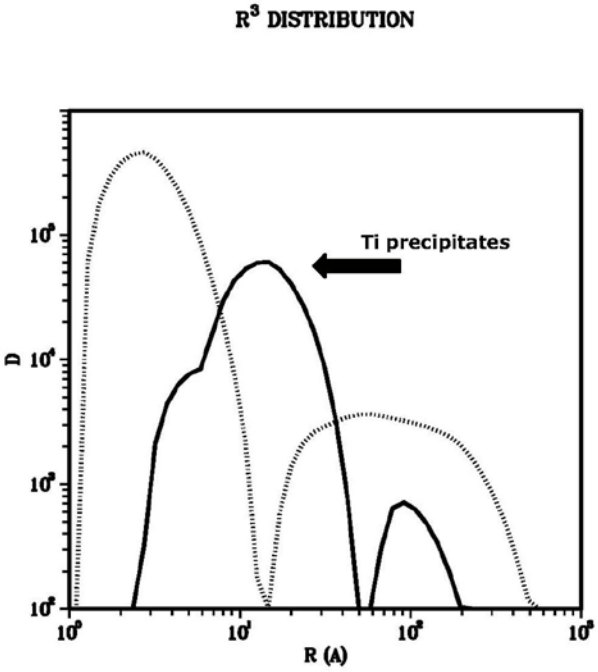

Fig. 5 – Distribuzioni dimensionali in unità arbitrarie (volume medio dei precipitati con dimensione tra R e R+dR in funzione di R, dove R è il raggio medio ottenute dai dati della fig. 4: la curva continua si riferisce al campione contenente 0.4 wt% Ti

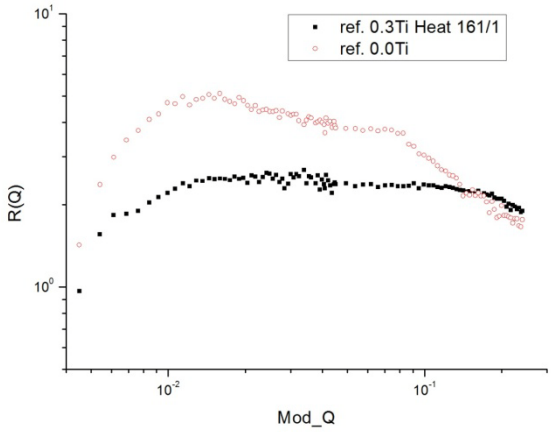

Fig. 6 – Rapporto R(Q) definito come in eq. (2) per i due campioni di fig. 4.

Riguardo all'effetto di trattamenti termici, la fig. 7 mostra le sezioni d'urto di diffusione neutronica ai piccoli angoli ottenute per una serie di campioni di acciaio 9 Cr 0.35 Y_2O_3 wt% invecchiati a 800°C per tempi compresi tra 720 h e 4320 h: ad una temperatura alla quale un acciaio ferritico/martensitico va soggetto a importanti trasformazioni microstrutturali anche per tempi molto più brevi di quelli considerati, il corrispondente materiale ODS appare non modificato nella sua microstruttura fine. Invece la fig. 8 mostra che a temperature molto più elevate (1330°C) anche un trattamento di sole 2 h modifica radicalmente la microstruttura del materiale, producendo la formazione di nuove fasi che sono in corso di identificazione.

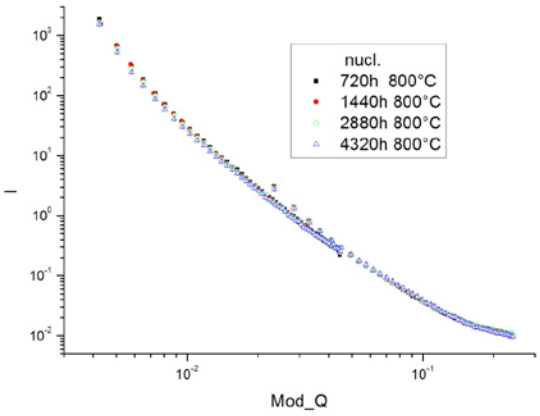

Fig. 7 - Sezioni d'urto di diffusione neutronica ai piccoli angoli (componente nucleare) dell'acciaio ferritico/martensitico 9 Cr 0.35 Y_2O_3 wt% sottoposto a invecchiamenti termici a 800°C

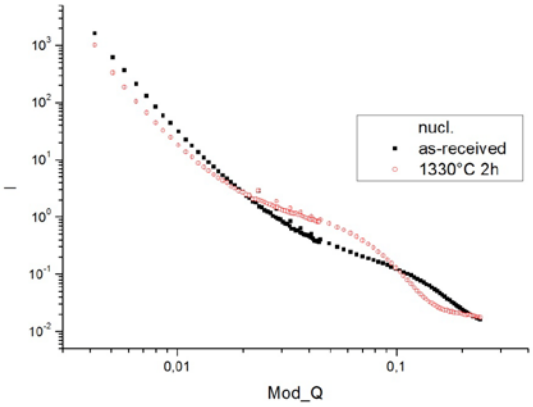

Fig. 8 -Ssezioni d'urto di diffusione neutronica ai piccoli angoli (componente nucleare) dell'acciaio ferritico/martensitico 9 Cr 0.35 Y_2O_3 wt% nello stato tal quale e dopo rinvenimento di 2 h a 1330°C

Riguardo ai materiali forniti dall'Università di Pechino, la fig. 9 (a-b) mostra le sezioni d'urto bidimensionali dell'acciaio ODS 9 Cr ferritico/martensitico (a) e 18 Cr austenico (b): pur essendo state le due misure eseguite in presenza di campo magnetico saturante, è evidente che l'acciaio austentitico è non-magnetico e presenta un diagramma di diffusione quasi perfettamente isotropo. La fig. 10 mostra il confronto tra le sezioni d'urto nucleari (parallele al campo magnetico) dei due campioni: la maggiore intensità osservata nel 9 Cr ferritico/martensitico è in prima ipotesi attribuita alle nano-particelle ceramiche, che si comportano come "buchi" non-magnetici in una matrice metallica (martensitica) magnetizzata a saturazione, producendo quindi un elevato fattore di contrasto a differenza di quanto avviene nel materiale austenitico. Tuttavia su questa ipotesi sono in corso accurate verifiche vista la complessità dei materiali studiati e la difficoltà di osservare in microscopia elettronica micro difetti di così piccola dimensione (1 nm).

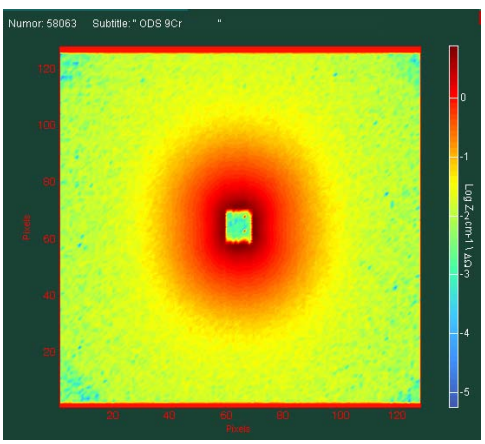

a)

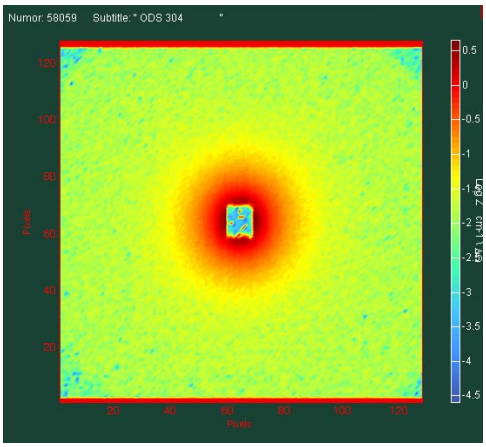

b)

Fig. 9 – Spettri bi-dimensionali di diffusione neutronica ai piccoli angoli per l'acciaio ODS ferritico/martensitico (a) e austenitico (b); il campo magnetico esterno è orizzontale nel piano nella figura

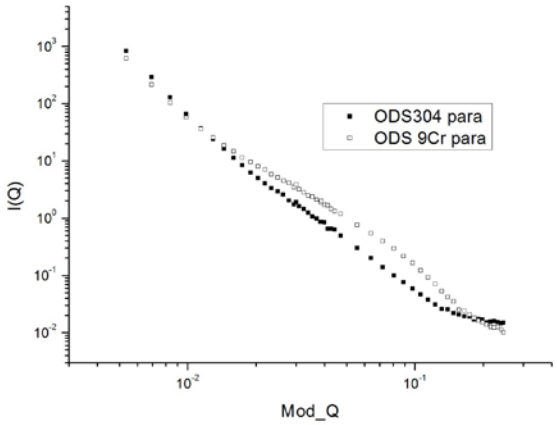

Fig. 10 - Sezioni d'urto di diffusione neutronica ai piccoli angoli (componente nucleare) dell'acciaio ODS ferritico/martensitico e austenitico

Oltre alle misure di diffusione neutronica ai piccoli angoli, è stata eseguita una serie di misure di diffrazione neutronica sia su due nanopolveri ODS 9 Cr 0.35 Y_2O_3 wt% invecchiate ad alta temperatura e fornite da KIT, sia su diversi campioni, policristallini e in forma di nanopolveri di acciai ODS ferritico/martensitici e austetitici forniti dall'Università di Pechino. Essendo tali misure state effettuate dall'ILL-Grenoble su contratto ENEA in ambito PAR 2011 si rimanda al rapporto tecnico di attività fornito dall'ILL e allegato al presente consuntivo per un elenco particolareggiato di tutti i risultati conseguiti. Le conclusioni di questo studio più significative ai fini dell'ottimizzazione dei trattamenti termo meccanici di produzione e della comprensione dell'evoluzione micro strutturale sono le seguenti:

- gli acciai ferritico/martensitici ODS hanno una struttura cristallografica di tipo bcc e gli austenitici di ti tipo fcc, come prevedibile, ma dopo un trattamento alligazione meccanica per produzione di polvere nano-strutturata l'acciaio austentico si trasforma in ferritico/martensitico con struttura quasi completamente di tipo bcc (fig. 11)

- l'analisi degli spettri di diffrazione, basata su metodo del rif. (6), non consente di identificare quantità della fase Y_2O_3 corrispondenti a quella nominale che, se effettivamente presente, lo è in misura ben inferiore o in forma non ben cristallizzata; analoghe conclusioni si traggono per le fasi $M_{23}C_6$ e Fe_3C, che pure si possono formare in questi acciai ma che non vengono rivelate entro il rumore di fondo

- viene invece identificata la fase TiN, come risulta dalla fig. 12; inoltre, tra i principali picchi delle fasi bcc e fcc dei due tipi di acciai studiati si osservano contributi al segnale nettamente superiori al rumore di fondo, certamente dovuti alla presenza di fasi cristallografiche che si sta cercando di identificare per completare la caratterizzazione metallurgica di base dei materiali studiati.

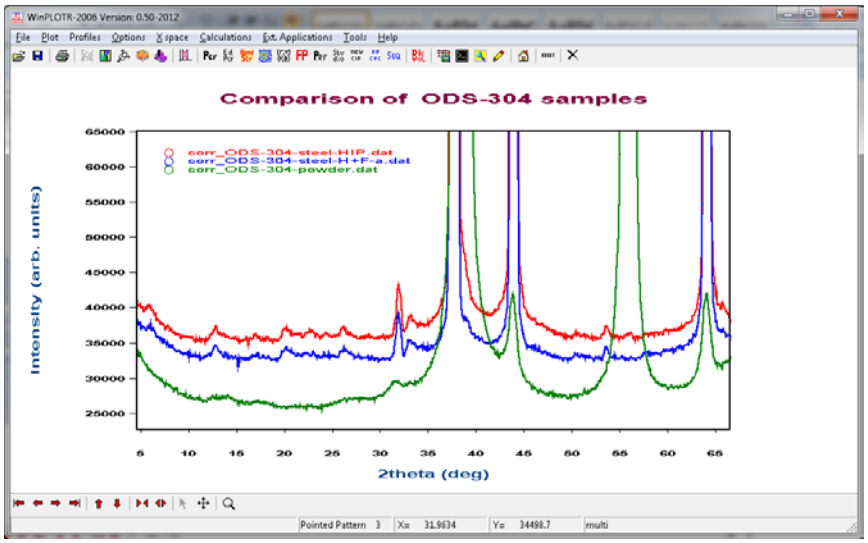

Fig. 11 – Diagrammi di diffrazione neutronica ottenuti dai campioni austenitici ODS 18 Cr sottoposto a pressa isostatica a caldo (rosso) , a successiva forgiatura (blu) e ad alligazione meccanica per produzione di nano polvere a struttura bcc (verde)

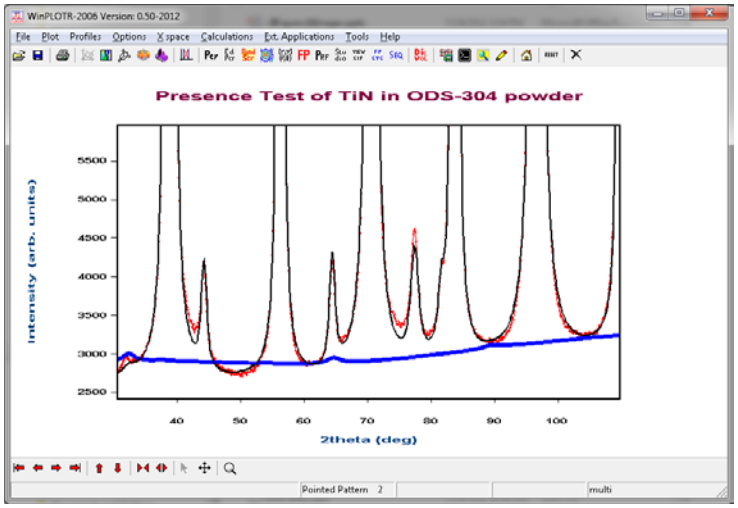

Fig. 12 – Diagramma di diffrazione neutronica ottenuto dal campione austenitico ODS 18 Cr (rosso) con contributo della fase TiN (blu)

Conclusioni

Le attività tecnico-scientifiche espletate nell'ambito della Linea Programmatica C1.e del PAR 2011 hanno consentito la realizzazione di un programma sperimentale di prove di diffusione e diffrazione neutronica, condotte in sinergia con EERA e IAEA e con la collaborazione di due importanti partner internazionali, volte a migliorare le conoscenze di base sugli acciai ODS per reattori di IV generazione. L'uso combinato della diffusione neutronica ai piccoli angoli e della diffrazione neutronica ha consentito di caratterizzare sia da un punto di vista microstrutturale sia da un punto di vista cristallografico l'effetto di trattamenti termo-meccanici su diversi tipi di acciai ODS, sia ferritico/martensitici sia austenitici. In sintesi, la microstruttura dei i materiali studiati appare stabile per temperature inferiori ai 1000°C ma estremamente sensibile a variazioni anche minime degli elementi di lega, che possono produrre nuove fasi di precipitati ancora non del tutto identificate. In particolare andranno approfondite le ricerche sull'esatta stechiometria della fase ceramica indurente e sull'effetto dei trattamenti termo-meccanici di produzione dei materiali. Questo studio ha inoltre consentito l'avvio di una metodologia sperimentale di sicuro interesse per la prosecuzione di queste ricerche e in generale per lo studio dei materiali nucleari.

Bibliografia

1) G. Kostorz "Neutron and X.ray Scattering" Ch. 12 in *Physical Metallurgy* pp 1115-1199. W. Cahn and P. Haasen Eds. 4TH Edition (1996).

2) M. T. Hutchings, C. G. Windsor, Industrial Applications, in Methods of Experimental Physics, vol 23-c, Neutron Scattering, K. Sköld & D. L. Price Ed.s, Academic Press (1987) p. 405

3) www.ill.eu

4) R. Coppola, R. Kampmann, M. Magnani, P. Staron, Acta Mat. 46 (1998) 5547

5)Hansen TC, Henry PF, Fischer HE, Torregrossa J, Convert P: , Measurement Science and Technology 19 (2008) 034001.

6)Rodriguez-Carvajal, J.Physica B.(1993), 192, 55.

7)A. Möslang, C. Adelhelm, R. Heidinger, Int. J. Mat. Res. 99 (2008) 10

8)R. Coppola, M. Klimiankou, R. Lindau, R. P. May, M. Valli, Physica B 350 (2004) 545

9)R. Coppola, R. Lindau, R. P. May, A. Möslang, M. Valli, P. Vladimirov, A. Wiedenmann, J. of Ph. C 251 (2010)012052

10)Z. Zhou, S. Yang, W. Chen, L. Liao, Y. Xu, J. N. Mat. , in corso di stampa

Allegato 1

Rapporto di attività ILL-Grenoble su misure eseguite per l'ENEA in ambito PAR 2011 LP1 C1.e

Report on the industrial experiment on steels at D20 (12 July 2012)

Juan Rodriguez-Carvajal
(version of 24 July 2012)

Brief description of the experiments

The experiments performed at D20 consisted of taking a series of diffraction patterns of different steel samples, either in form of cylindrical ingots of in form of powders. The conditions of the experiments were the following:

- D20 in high resolution mode (monochromator take-off angle ~118°), wavelength ~1.36Å
- Sample containers: vanadium cans of 7mm or 9mm
- The samples were always placed under vacuum.
- The data collection was done during the necessary time to get the appropriate statistics.
- Some detector cells were behaving abnormally in well defined angular regions but this has a minor effect on the data treatment. A correction has been performed for some of the bad behaving cells.
- All data were treated using the programs of the FullProf Suite (FullProf, WinPLOTR, etc.).

In the first part of this document the data have been treated using the main present phase using the Rietveld method or Le Bail fits. In a second part we have attempted to determine quantitatively the minor phases present in the samples. For more details concerning the values of all parameters and indicators resulting from the refinements consult directly the output files of the programs.

Calibration of the diffractometer

The diffraction pattern of the standard sample Na-Ca-Al-F was taken in order to prepare an instrumental

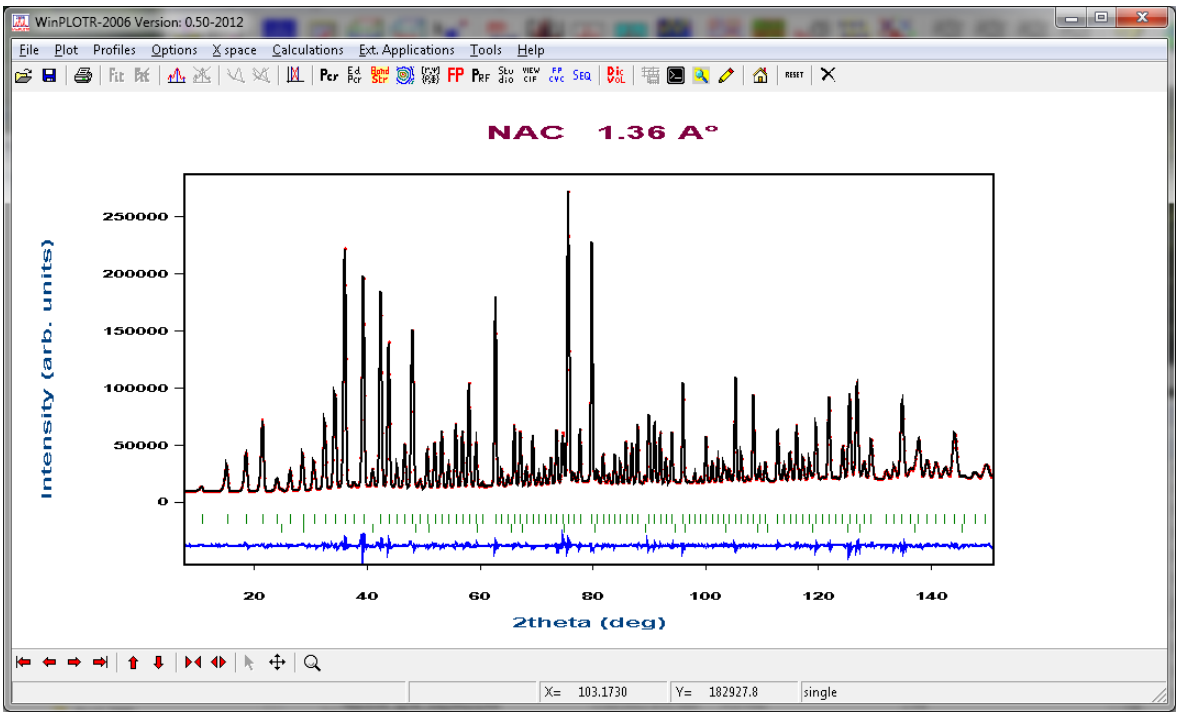

Figure 1: Observed and calculated pattern of the calibration sample $Na_2Ca_3Al_2F_{14}$.

resolution function file according to the conditions of the experiment. This allows the possibility to obtain micro-structural information directly from the Rietveld treatment of the data.
The Rietveld refinement of the data, fixing the crystal structure and cell parameters, and refining the U,V,W,X parameters as well as the scale factor, the background parameters and the zero-shifts, wavelength and sample displacement parameters give the final result shown in Figure 1.

The instrumental resolution file constructed from the refined data is shown below.

```
! Resolution Function of D20 obtained from  Na2Ca3Al2F14 (lambda=1.36 angstroms) ireso    1
! To be used with IRESO=1 in FullProf.2k (version > 2.4)
! File: corr_NaCalAlF-9mm-July2012 11-Jul-12,  treated Date: 19-07-2012
! d20 11-Jul-12 12:57:31 User Coppola  L.C.Carvaja Run 802128*d20_2012_06_7930
!      Lambda1  Lambda2   Ratio(I2/I1)
WAVE  1.357911 1.357911  0.00000
!    NPROF    Shape1    Shape2   Shape3
PROF    7        0.0       0.0      0.0
!  Cos(2thM)^2 for polarization = 0 for neutrons
CTHM  0.0
!     2theta-min   step   2theta-max
THRG     1.0       0.100     170.00
!          S_L      D_L
ASYM    0.06435   0.04445
!   Uins       Vins       Wins       Xins       Yins       Zins
   0.140393  -0.308571   0.265235   0.046647   0.000000   0.000000
```

Panel 1: Instrumental resolution function file used in the data treatment and extracted from the refinement of the Na-Ca-Al-F data.

This file is read by FullProf, when required by the input control file (PCR-file), and the broadening of the experimental peaks is interpreted in terms of micro-structural parameters (see FullProf manual).
The used PCR file can be provided on request.

Measured samples

The following samples, in addition of a background calibration, were measured in D20

#	Sample	Designed Compositions	quantity	size
A1	ODS-304	Fe-18Cr-8Ni-1Mo-0.15Si-0.3N-0.35Y_2O_3-0.5Ti MA+HIP (1150℃, 3h)	1	Φ10×8mm steel HIP
A2	ODS-304	Fe-18Cr-8Ni-1Mo-0.15Si-0.3N-0.35Y_2O_3-0.5Ti MA+HIP (1150℃, 3h)+Forging	1	Φ10×10mm steel H+F
A2’	ODS-304	Same as above but, rotated 90° (texture)		
A3	ODS-304	Fe-18Cr-8Ni-1Mo-0.15Si-0.3N-0.35Y_2O_3-0.5Ti	1	MA powder
B1	9Cr-ODS	Fe-9Cr-1.5W-0.15Si-0.35Y_2O_3-0.5Ti MA+HIP (1150℃, 3h)+Forging	1	Φ10×10mm steel
B2	9Cr-ODS	Fe-9Cr-1.5W-0.15Si-0.35Y_2O_3-0.5Ti	1	MA powder
C1	HXN 950	1150℃ 2h	1	powder
C2	HXN 950	1050℃ 2h	1	powder
C3	HXN 950	950℃ 2h	1	powder

D1	Na-Ca-Al-F	Calibration sample	1	powder

The numbers (numors) of the associated data in the ILL database are the following

#	Sample	Numors
A1	ODS-304 steel HIP	802129-802133
A2	ODS-304 steel H+F	802138-802141
A2’	ODS-304 steel H+F rotated	802142-802145
A3	ODS-304 MA powder	802134-802137
B1	9Cr-ODS steel	802115-802118
B2	9Cr-ODS powder	802119-802122
C1	HXN 950	802146-802148
C2	HXN 950	802149-802151
C3	HXN 950	802152-802154
D1	Na-Ca-Al-F	802123-802128

PART 1

Data treatment of 9Cr-ODS samples B1 and B2

The measured neutron diffraction patterns of the samples corresponding to the samples B1 and B2 are shown in Figures 2 to 5, in which different zones and zooms are applied to emphasize the differences in the patterns.

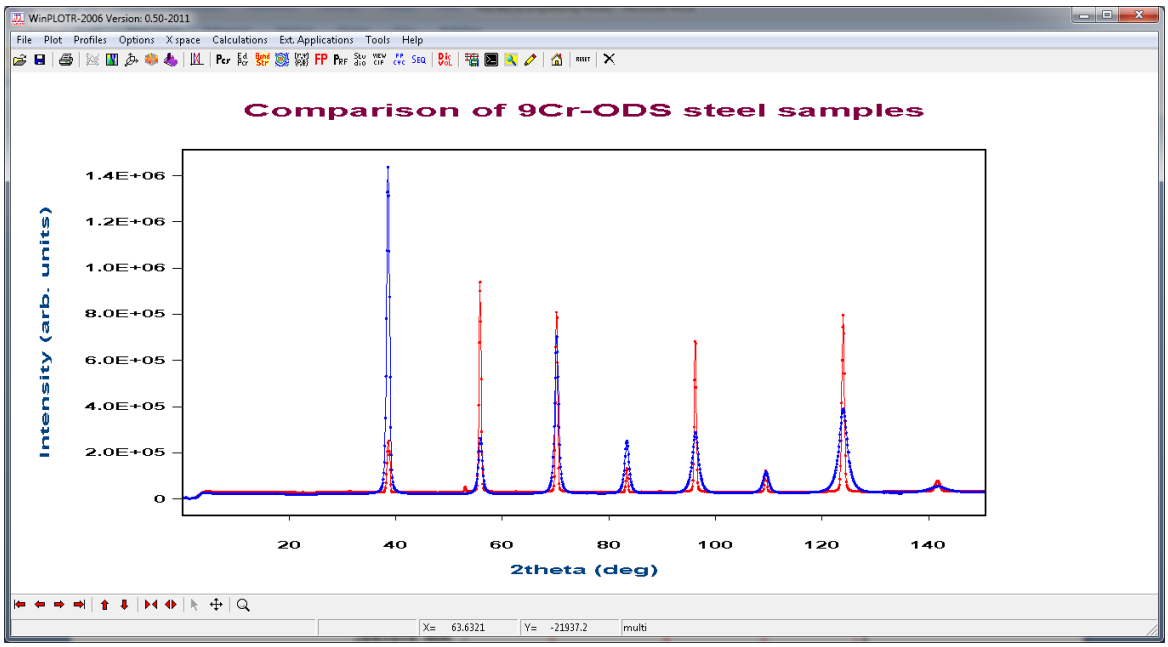

Figure 2: Global comparison of the diffraction patterns of 9Cr-ODS samples B1 (steel, in red) and B2 (powder, in blue). Notice that the powder sample has much more broad peaks than the ingot steel sample.

Both samples present the same average structure corresponding to that of ferrite (α-Fe), however additional minor (precipitate) phases are seen by making a zoom in the patterns to emphasize what is rising above the background. In that sense the Figure 3 clearly shows the presence of additional phases.

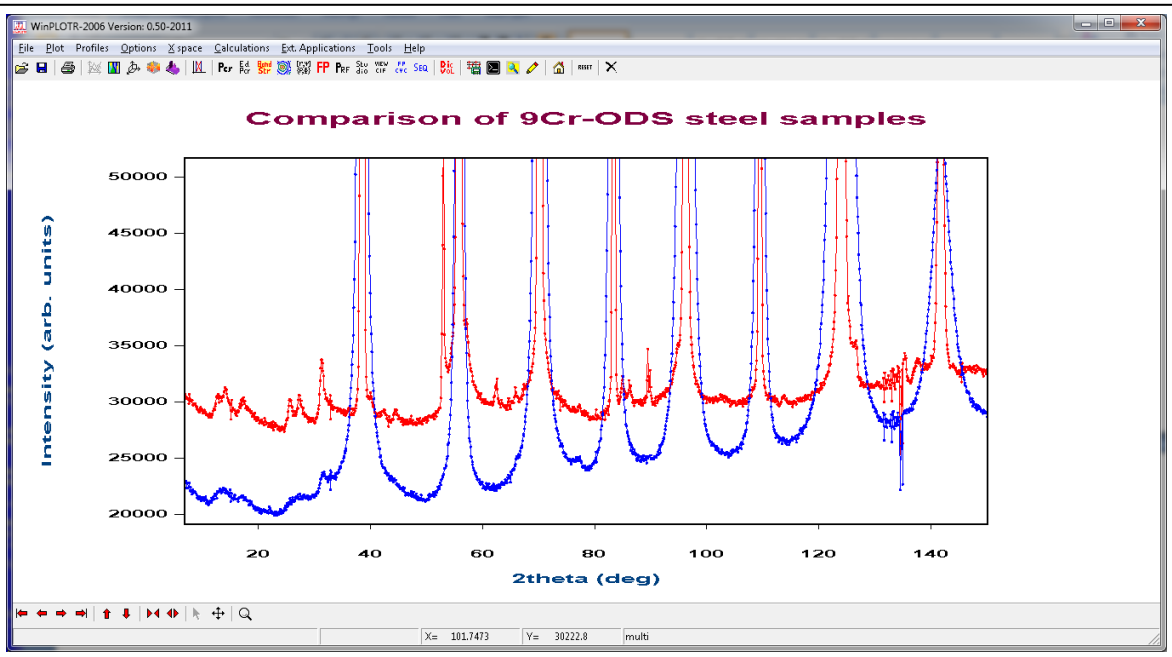

Figure 3: Comparison of the diffraction patterns of 9Cr-ODS samples B1 (steel, in red) and B2 (powder, in blue) emphasizing the regions just above the background. Notice that some detector cells between 130°-135° in 2θ, are not well corrected. In subsequent data treatment the cells have been corrected.

One can observe also that the intensities of the peaks are quite different. The reason is clearly that the ingot B1 sample presents a strong preferred orientation (texture) preventing the treatment using de Rietveld method. However, a refinement of the full pattern can be performed using the Le Bail fit in which the integrated intensities of the peaks are not fixed by the crystal structure. This permits to analyse the micro-structural parameters of the sample.

Introducing the average structure of ferrite α-Fe, with a composition close to nominal (notice that we cannot determine de composition using the Rietveld method because there is a single site occupied by different atoms and there is a correlation of 100% with the scale factor), and using the instrumental resolution function determined with the standard sample Na-Ca-Al-F (D1), we obtain the results shown in Figure 4 after refining overall scale and temperature factors, cell parameters, background coefficients (Chebychev polynomial) and micro-structural parameters.

In Table I we have gathered the most important numerical parameters together with their standard deviations.

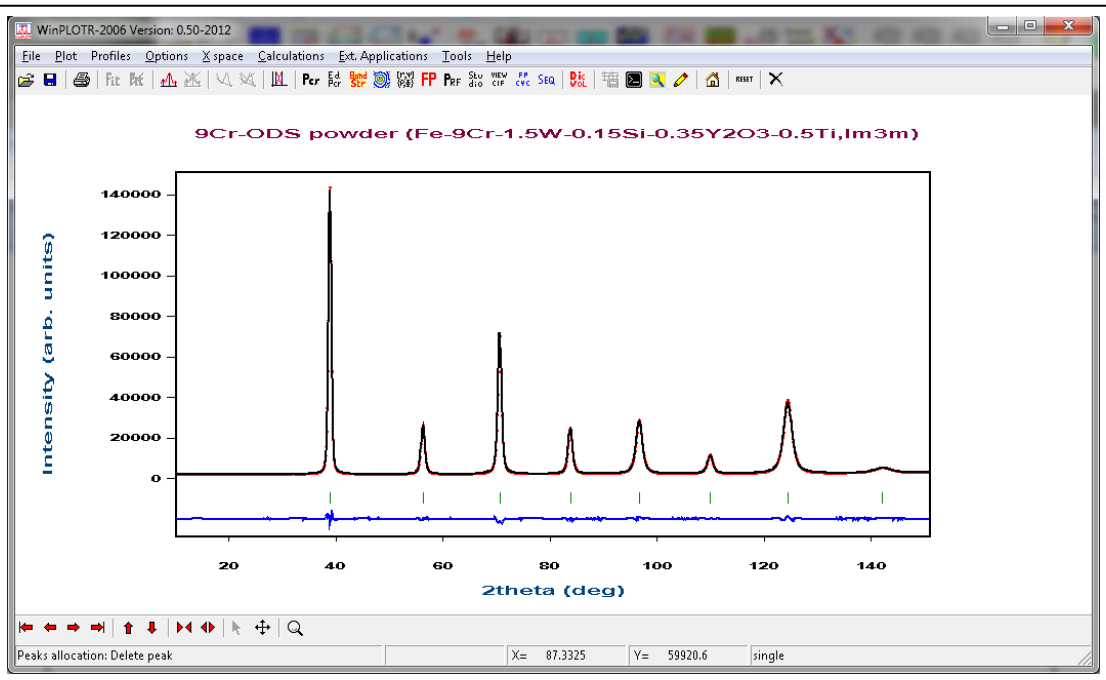

Figure 4: Rietveld refinement of the 9Cr-ODS sample B2 (powder) using the average α-Fe structure (space group Im3m).

The case of the B1 sample cannot be treated using the Rietveld method due to the strong texture observed in the sample. We have used in this case the Le Bail method. The results are shown in Figure 5.

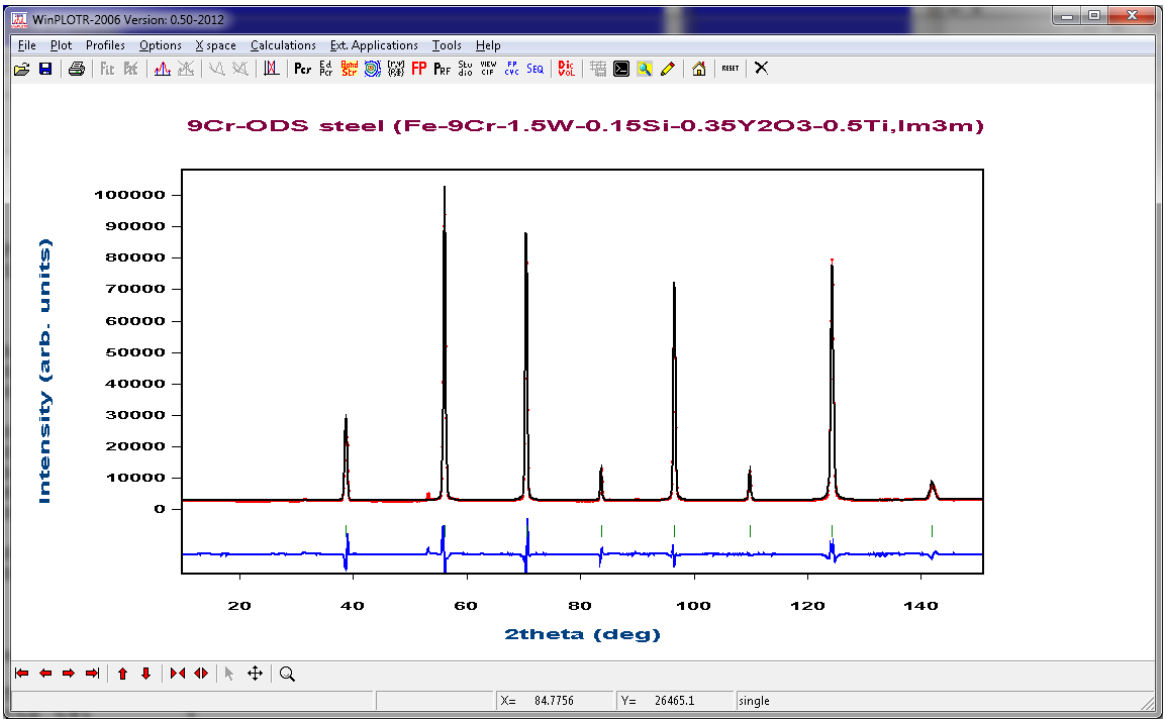

Figure 5: Le Bail fit of the 9Cr-ODS sample B1 (ingot) using the average space group Im3m to generate reflections. The integrated intensities are refined in this process. Notice that the intensities are not the same as those of the powder sample due to the strong texture.

```
 =>  No. of reflections for pattern#:   1:     8

  ==> PROFILE PARAMETERS FOR PATTERN#  1

  => Cell parameter: 2.87324(29) Å
  => overall scale factor   :    2.8496(74)
  => Overall tem. factor    :    0.420(5) Å²
  => Halfwidth parameter U :    0.075(45)
  => Generalized S_HKL strain parameters ==>
  =>   S_400: 188(11)      S_220:  3(11)
  => Lorentzian-Anisotropic-Strain Mixing Parameter: 0.55(2)

 ==> GLOBAL PARAMETERS FOR PATTERN#  1
  => Zero-point                 :  -0.07(4)
  => Cos(2theta)-shift parameter :  -0.09(3)
  => Sin(2theta)-shift parameter :  -0.40(2)
  => Chebychev Polynomials Background Parameters ==>
      22930(81); 3075(156); 2092(133);  508(123);  219(87);  266(78)

 ==> RELIABILITY FACTORS WITH ALL NON-EXCLUDED POINTS FOR PATTERN:  1
 => Cycle:  2 => MaxCycle: 19
  => N-P+C:  1389
  =>  R-factors (not corrected for background) for Pattern:  1
  => Rp:  2.41     Rwp:  3.13     Rexp:    0.44 Chi2:  51.3      L.S. refinement
  => Conventional Rietveld R-factors for Pattern:  1
  => Rp:  4.23     Rwp:  4.62     Rexp:    0.64 Chi2:  51.3
  => Deviance:  0.706E+05     Dev*  :   50.82
  => DW-Stat.:    0.2097     DW-exp:     1.8568
  => N-sigma of the GoF: 1325.628

  => Bragg R-factor:   1.46       Vol:   23.720( 0.004)  Fract(%):  100.00( 0.37)
  => Rf-factor= 0.819             ATZ:      259122.109   Brindley:  1.0000

               CPU Time:     0.516 seconds
                             0.009 minutes
 => Run finished at:     Date: 20/07/2012  Time: 09:11:57.601
```

It may be noticed that the refinement is not as good as that of the powder sample. This is due to the presence of big grains that give rise to a peak shape that is not as smooth as for a random powder.

Table II: Comparison of samples B2 (ODS-9Cr-powder) and B1(ODS-9Cr-steel)

```
 ==> PROFILE PARAMETERS         Powder            Steel Ingot
 => Cell parameter        :    2.87324(29)        2.88037(26) Å
 => overall scale factor  :    2.8496(74)         non-applicable
 => Overall tem. factor   :    0.420(5) Å²        non-applicable
=> Halfwidth parameter U :    0.075(45)          0.0   FIXED
=> Halfwidth parameter Y :    0.0 FIXED          0.054(1)
 => Generalized S_HKL strain parameters ==>
 =>   S_400: 188(11); S_220: 3(11)          S_400: 0.0; S_220:0.0 FIXED to zero for Steel Ingot
 => Lorentzian-Anisotropic-Strain Mixing Parameter: 0.55(2)

==> GLOBAL PARAMETERS                  Powder             Steel Ingot
 => Zero-point                 :       -0.07(4)            0.565(42)
 => Cos(2theta)-shift parameter :       -0.09(3)           -0.441(25)
 => Sin(2theta)-shift parameter :       -0.40(2)           -0.778(23)
 => Chebychev Polynomials Background Parameters ==>
     22930(81) ; 3075(156); 2092(133);  508(123);  219(87 );  266(78)                  Powder
     30428(198);  907(394); 1666(330);   13(306);  755(213); -223(190)                 Steel Ingot
```

However, the cell parameters and micro-structural parameters can be reliably been obtained as seen in Table II. From the point of view of the micro-structure, the diffraction pattern of the B1 does not show broadening with respect to the instrumental resolution. Only a small Lorentzian size effect can be refined Y=0.054(1) corresponding to an isotropic coherence domains of apparent (volume averaged) size of D_{app}≈91.3 nm. If we consider that the shape of the coherence domains is spherical the corresponding diameter is D=4/3 D_{app}≈122 nm.

The powder sample B2, shows a micro-structure characterised by the presence of anisotropic micro-strains, most probably due to the presence of a high density of dislocations. The refined broadening of the peaks (through the parameters S_{400} and S_{220}, see the manual of FullProf for references), obtained from the automatically generated microstructure file, is shown in Table III.

Table III: Micro-structural information of samples B2 (ODS-9Cr-powder) and B1(ODS-9Cr-steel) obtained from the respective MIC files.

(B2)

h	k	l	2θ°	s=1/d(Å^{-1})	HGo(°)	HGi(°)	HLo(°)	HLi(°)	beta_TCH	strain(10^{-4})
1	1	0	39.0458	0.4922	0.4609	0.4165	0.2294	0.0165	5.5752	56.6097
2	0	0	56.4073	0.6961	0.5434	0.3743	0.4783	0.0250	10.8264	77.7376
2	1	1	70.7355	0.8525	0.5225	0.3420	0.4592	0.0331	9.6566	56.6097
2	2	0	83.8823	0.9844	0.5928	0.3183	0.5813	0.0419	11.1504	56.6097
3	1	0	96.7066	1.1006	0.8205	0.3095	0.9140	0.0525	15.6050	70.8651
2	2	2	109.8855	1.2056	0.7643	0.3326	0.7678	0.0665	11.4589	47.4976
3	2	1	124.2981	1.3022	1.1373	0.4291	1.2243	0.0883	14.7506	56.6097
4	0	0	141.8927	1.3922	2.2517	0.7407	2.5826	0.1351	21.6529	77.7376

(B1)

h	k	l	2θ°	s=1/d(Å^{-1})	HGo(°)	HGi(°)	HLo(°)	HLi(°)	beta_TCH	App-Size(Å)
1	1	0	38.9451	0.4910	0.4168	0.4168	0.0740	0.0165	1.0945	913.52
2	0	0	56.2551	0.6944	0.3747	0.3747	0.0864	0.0249	1.0945	913.52
2	1	1	70.5342	0.8504	0.3424	0.3424	0.0994	0.0330	1.0945	913.52
2	2	0	83.6275	0.9820	0.3187	0.3187	0.1145	0.0417	1.0945	913.52
3	1	0	96.3879	1.0979	0.3094	0.3094	0.1335	0.0522	1.0945	913.52
2	2	2	109.4820	1.2027	0.3311	0.3311	0.1599	0.0660	1.0945	913.52
3	2	1	123.7633	1.2990	0.4236	0.4236	0.2023	0.0873	1.0945	913.52
4	0	0	141.0792	1.3887	0.7186	0.7186	0.2947	0.1320	1.0945	913.52

The meaning of the different columns is explained in detail in the MIC files. Size contribution is negligible in the powder sample because the broadening is dominated by the anisotropic strains. The small contribution of the isotropic strain (see half-width U-parameter in tables I and II) is taken into account in the calculation of beta. In the sample B1, the opposite happens: only a small Lorentzian contribution, coming from the coherence diffraction domains, give rise to the broadening of the peaks.

HGo and HLo are the total Gaussian and Lorentzian FWHM of the peaks, HGi and HLi are the instrumental Gaussian and Lorentzian FWHM of the instrument contribution. The parameter beta_TCH is the intrinsic integral breadth of the peak from which we obtain the strain and size parameters (see the manual of FullProf to get the information about the details of calculations).
As explained in the header of the MIC files the strain values correspond to the so called "maximum strain" (see for instance the chapter 7 by D. Baltzar of "Defect and Microstructure Analysis by Diffraction") and have no units. The expressions for calculating the apparent size and strains, for each Bragg reflection, are:

$$D_{app} = \frac{\lambda}{\beta_{size}\cos\theta} = \frac{1}{\beta^*_{size}} \qquad e = \frac{1}{2}\beta^*_{strain} d = \frac{\beta^*_{strain}}{2s} = \frac{\beta_{strain}\cos\theta}{2s\lambda}$$

In which the integral breadths (without "*") are expressed in radians and the integral breadth with a "*" symbol are expressed in reciprocal space ($Å^{-1}$), they are already corrected from instrumental resolution.

To visualise how the anisotropic strain is in the crystal space one can use the program GFourier to make a projection of the surface constructed by the points of the space that for a particular direction the distance to the origin is the value of the strain in that direction. The surface is simply constructed by separating the space with two values: zero outside the surface and a constant value for the points at the interior of the surface. For isotropic strains this surface is a sphere. The projection has a different colour

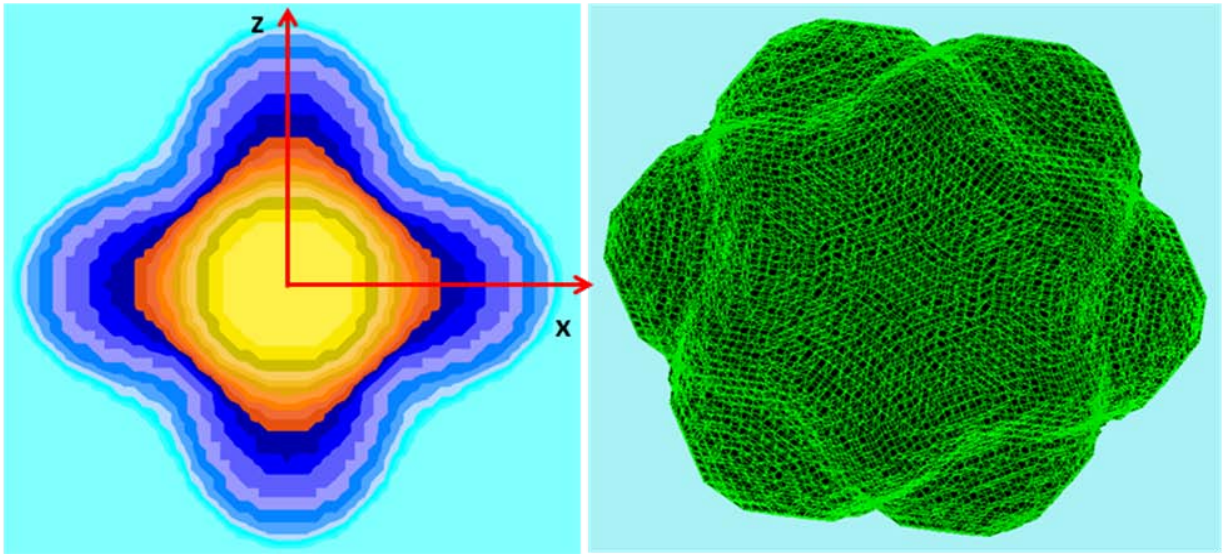

Figure 6: Micro-strain pattern of sample B2 (ODS-9Cr-powder). On the left a projection of the strain surface is represented on the x-y plane. On the right a pseudo-3D representation of the strain surface is shown with a point of view along nearly [111]. The surface has a shape similar to a deformed rounded octahedron.

(value) on each point because it is obtained by summing the density of the pixels in the columns parallel to the projection direction. The strain surface for the sample B2 is represented in Figure 6.

Data treatment of ODS-304 samples A1, A2, A2' and A3

The measured neutron diffraction patterns of the samples corresponding to the samples A1 to A3 are shown in Figures 7 to 12, in which different zones and zooms are applied to emphasize the differences in the patterns.

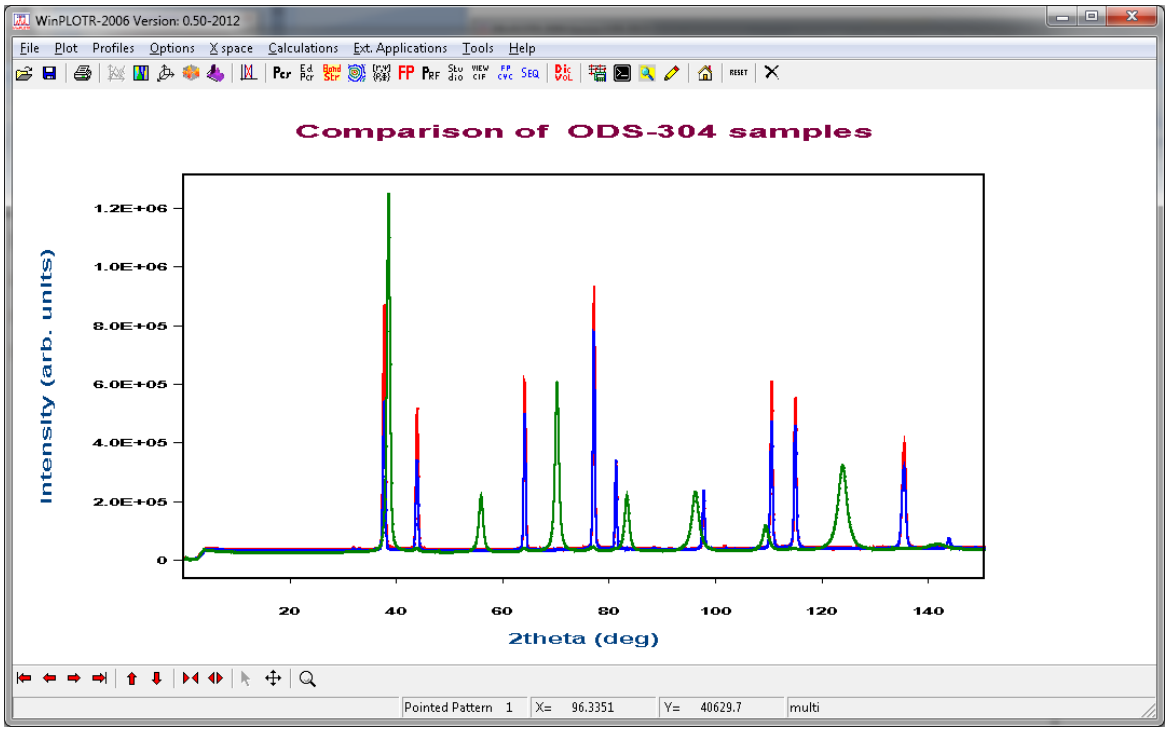

Figure 7: Global comparison of the diffraction patterns of ODS-304 samples A1(HIP), A2(H+F) (steel, in red and blue) and A3 (powder, in green). As in the previous cases, notice that the powder sample has much more broad peaks than the ingot steel sample, and for these samples the average structure has changed from Fm3m (steels) to Im3m (powder).

As a proof of the strong texture of the ingots, we present in Figure 8, the comparison of the diffraction patterns of the sample A2 with the pattern obtained on the same (now called A2') by just rotating 90° approximately around the optic centre of the diffractometer.

The most important consequence of the mechanical alloying for producing the powders with the same composition as the ingots is that the average structure of the powder (A3) corresponds to the structure of α-Fe (Im3m, ferritic steel) whereas the structure of the ingots (A1, A2) corresponds to austenite (Fm3m, austenitic NiCr-steels).

It may be notice that the powder sample is not a pure ferrite sample, it contains as a minor phase the austenite phase. This can be seen in Figure 9, in which we show a zoom of the zone emphasizing the regions just above the background.

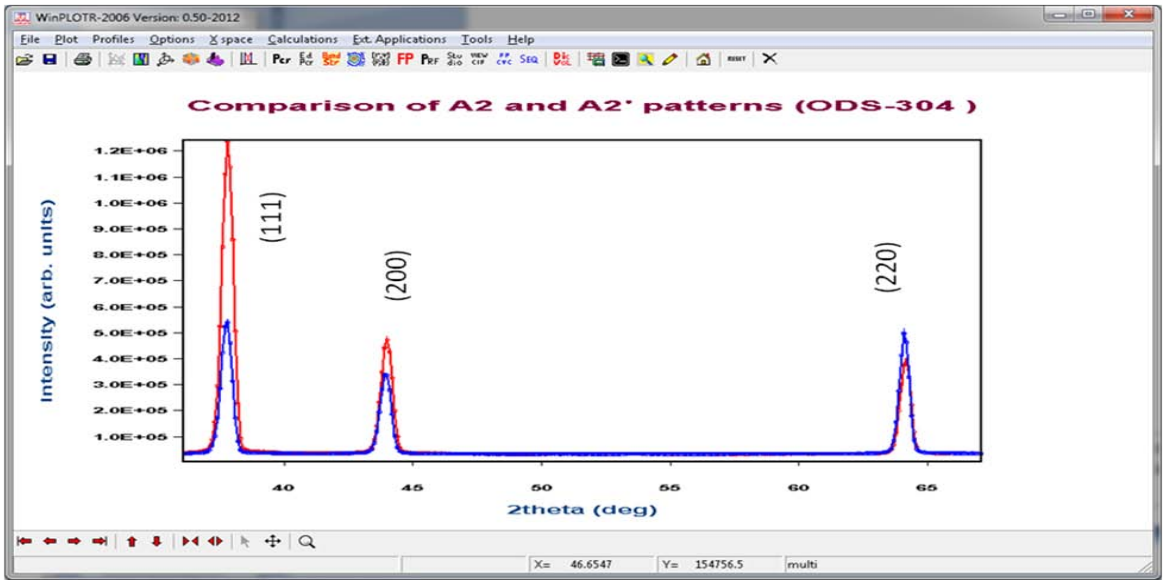

Figure 8: Portion of the diffraction patterns of the sample A2(H+F) (A2 and A2') obtained by a rotation of 90° around the omega axis of the diffractometer. The change in intensities indicates the presence of strong texture effects.

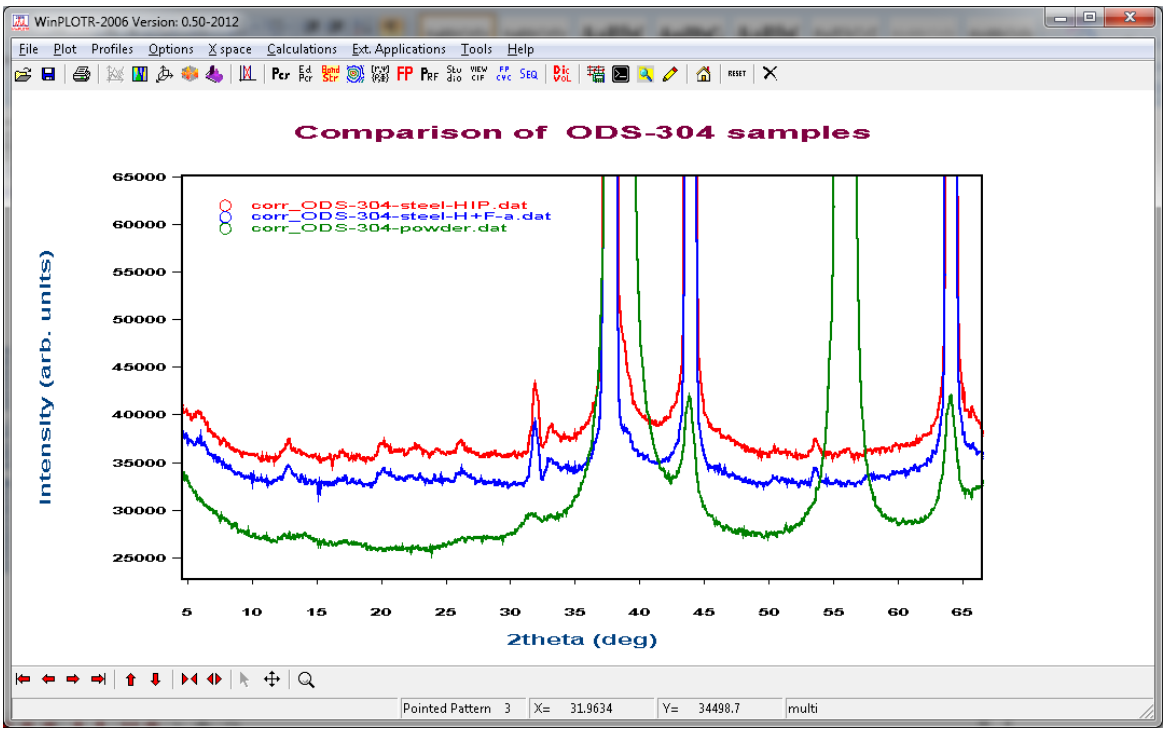

Figure 9: Comparison of the diffraction patterns of ODS-304 samples A1(HIP), A2(F+F) (steel, in red and blue) and A3 (powder, in green) emphasizing the regions just above the background in the low angle part. Notice that in the powder sample it exist an austenitic component together with the major ferritic component.

We have applied the same method as that used for the B1-B2 samples to analyse the data. Only the powder diffraction pattern can be treated using the Rietveld method. For the ingot samples (A1-A2) only the Le Bail fit can be done. In the following two figures (10 and 11) the results of the Rietveld refinement

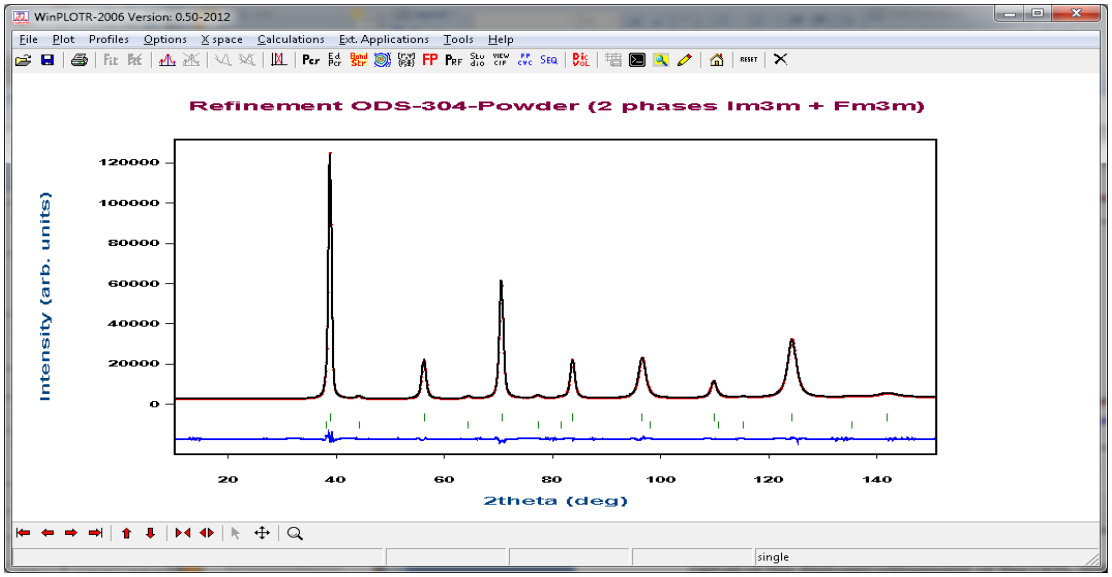

Figure 10: Rietveld refinement of the ODS304 sample A3 (powder) using the average α-Fe structure (space group Im3m, first row of tick marks) plus a minor component crystallising in the austenite structure (space group Fm3m, second row of tick marks).

of the powder sample are shown.

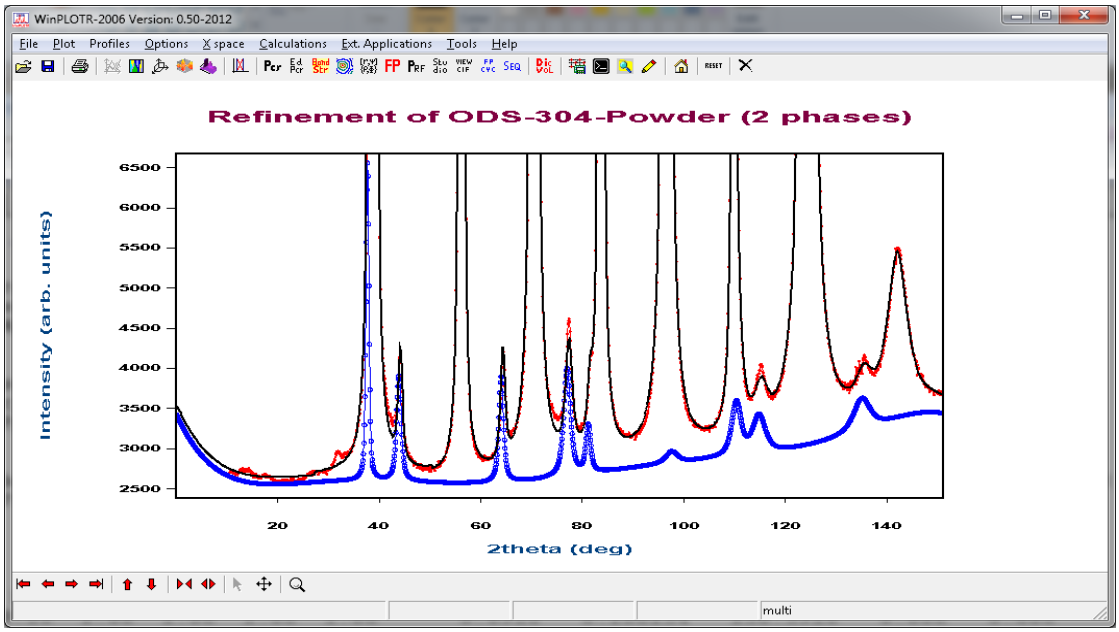

Figure 11: Contribution of the minor austenitic phase (in blue) superimposed to the total pattern. The black curve is the calculated pattern and the red curve is constituted by the observed diffraction pattern.

In Table IV we have gathered the most important numerical parameters together with their standard deviations.

Table IV: Summary of refinement parameters of sample A3 (ODS-304, MA powder). Some profile parameters have been constrained to be the same in both phases (in red)

```
 => PCR file code: ODS-304-pwd
 => DAT file code: corr_ODS-304-powder. -> Relative contribution: 1.0000
 => Title:   ODS-304 powder (Im3m + Fm3m phases)

 ==> RESULTS OF REFINEMENT:
=> No. of fitted parameters:   20
=> No. of reflections for phase#1:  8
=> No. of reflections for phase#2: 11

 ==> PROFILE PARAMETERS FOR PATTERN#  1

 => Phase No.  1 FeCrNiMoTi_Fm3m                        I m -3 m
 => Cell parameter        :    2.87427(29) Å
 => overall scale factor  :    2.8856(64)
 => Overall tem. factor   :    0.479(5) Å²
 => Halfwidth parameter U :    0.07(2)
 => Generalized S_HKL strain parameters ==>
 =>   S_400: 244(9)      S_220:  -74(6)
 => Lorentzian-Anisotropic-Strain Mixing Parameter: 0.64(2)

=> Phase No.  2 NiCr_Fm3m                              F m -3 m
 => Cell parameter        :    3.59648(43) Å
 => overall scale factor  :    0.0374(5)
 => Overall tem. factor   :    0.479(5) Å²
 => Halfwidth parameter U :    0.07(2)
 => Generalized S_HKL strain parameters ==>
 =>   S_400: 244(9)      S_220:  -74(6)
 => Lorentzian-Anisotropic-Strain Mixing Parameter: 0.64(2)

==> GLOBAL PARAMETERS FOR PATTERN#  1
 => Zero-point                :  -0.09(4)
 => Cos(2theta)-shift parameter :  -0.07(3)
 => Sin(2theta)-shift parameter :  -0.40(2)
 => Chebychev Polynomials Background Parameters ==>
     30165(152); 2383(303); 3464(269); -1234(240);  942(190); -926(154); 496(99); -648(82)

==> RELIABILITY FACTORS WITH ALL NON-EXCLUDED POINTS FOR PATTERN:  1
 => Cycle:  1 => MaxCycle: 19
 => N-P+C:  1385
 => R-factors (not corrected for background) for Pattern:  1
 => Rp:  1.79     Rwp:  2.33     Rexp:    0.42 Chi2:  31.1      L.S. refinement
 => Conventional Rietveld R-factors for Pattern:  1
 => Rp:  3.65     Rwp:  3.86     Rexp:    0.69 Chi2:  31.1
 => Deviance:  0.429E+05     Dev*  :   31.00
 => DW-Stat.:    0.3284     DW-exp:     1.8627
 => N-sigma of the GoF:  792.714

=> Phase:  1     ODS-304 powder Im3m
 => Bragg R-factor:   1.29       Vol:   23.746( 0.004)  Fract(%):   95.17( 0.30)
 => Rf-factor= 0.550             ATZ:      232462.734   Brindley:  1.0000

 => Phase:  2     ODS-304 powder Fm3m
 => Bragg R-factor:   2.49       Vol:   46.519( 0.010)  Fract(%):    4.83( 0.07)
 => Rf-factor=  1.11             ATZ:      464925.469   Brindley:  1.0000

              CPU Time:     0.422 seconds
                            0.007 minutes

 => Run finished at:     Date: 22/07/2012  Time: 10:27:37.190
```

The amount of the austenitic phase is close to 5% and the microstructure has been constrained to be the same as the predominant ferritic phase because the parameters cannot be refined in a stable manner due to the small contribution to the whole diffraction pattern.

As before, and due to the strong texture effects, the treatment of the samples in form of ingots can be done only by using the Le Bail method in which the integrated intensities of the reflections are free parameters. In figures 12 to 14 we show the final refinements of the diffraction patterns of samples A1 A2 and A2'. In all cases there is a single major phase that, in this case, corresponds to austenite Fm3m.

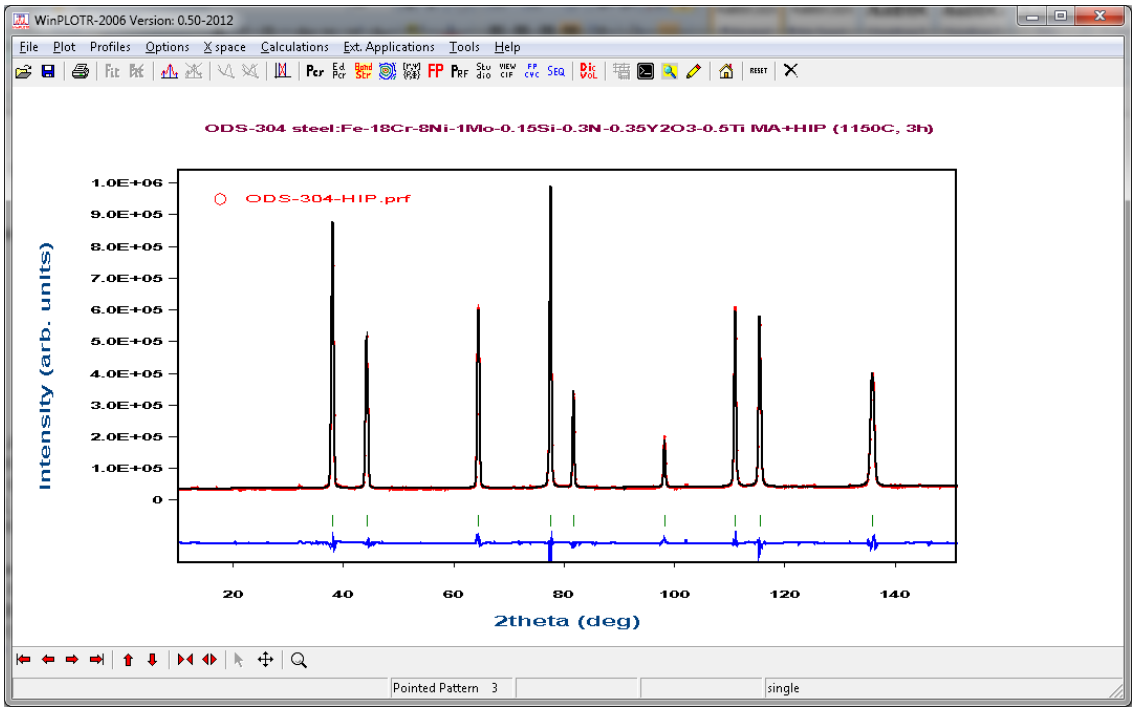

Figure 12: Le Bail fit of the ODS-304 sample A1, Fe-18Cr-8Ni-1Mo-0.15Si-0.3N-0.35Y_2O_3-0.5Ti, MA+HIP (1150°C, 3h, ingot) using the average space group Fm3m to generate reflections. The integrated intensities are refined in this process.

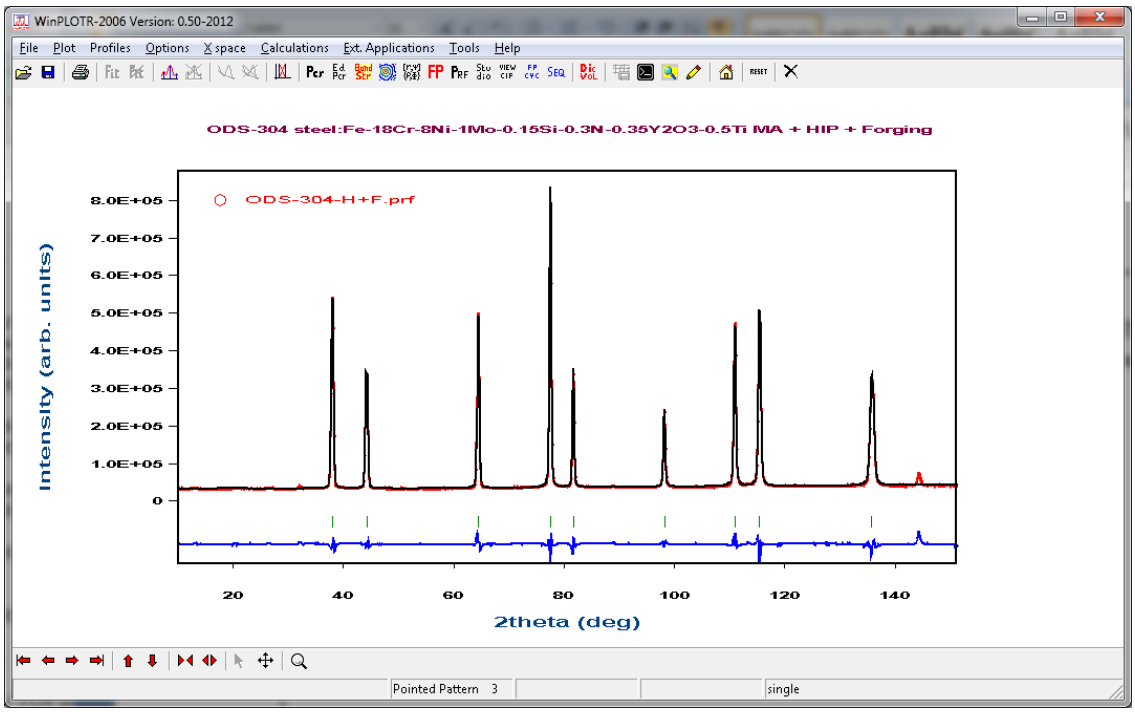

Figure 13: Le Bail fit of the ODS-304 sample A2, Fe-18Cr-8Ni-1Mo-0.15Si-0.3N-0.35Y_2O_3-0.5Ti, MA+HIP+Forging (1150°C, 3h, ingot). Notice the presence of a small peak at high angle of unknown origin.

As in the previous case, the micro-structural parameters have been fixed to zero, except for a small Lorentzian component due to size effects, for samples A1 and A2, and an additional isotropic strain for sample A2.

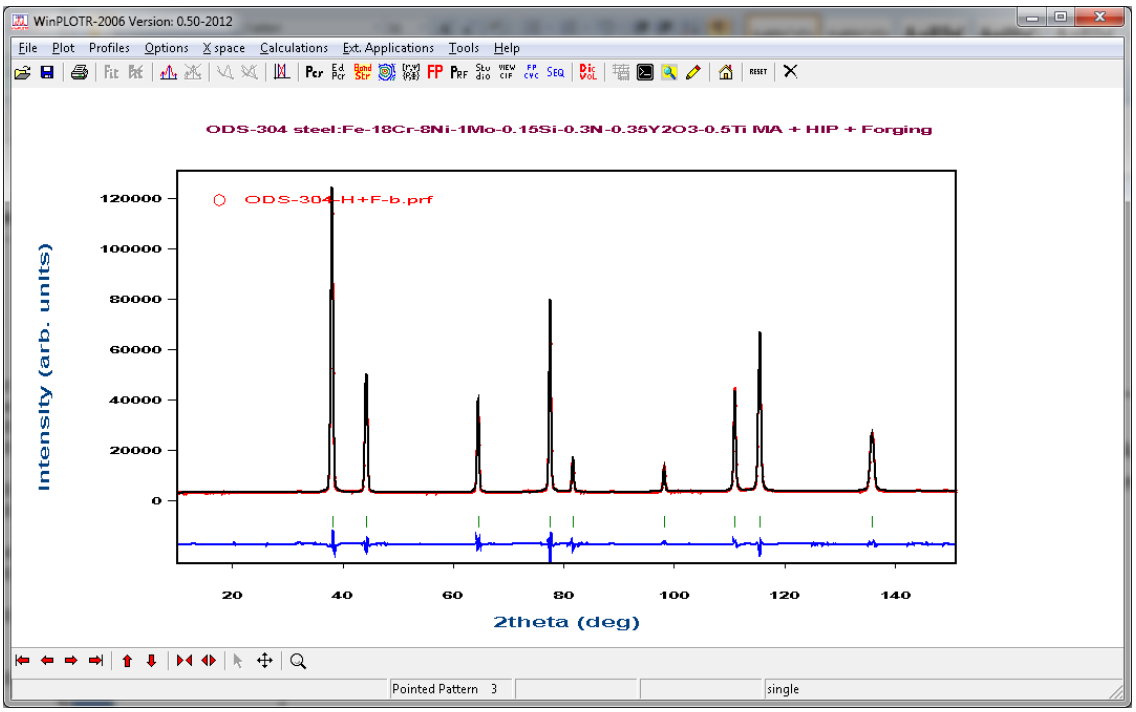

Figure 14: Le Bail fit of the ODS-304 sample A2'. It is exactly the same sample as A2 except that the diffraction pattern has been obtained by rotating the sample 90 approximately. Notice that the small peak at high angle in Figure 13 is nearly invisible.

In table V we show the results for the different reflections as obtained from the MIC files.

The sample A1 gives peaks slightly more Lorentzian than those of the instrument. This component, corresponding to Y= 0.0410(6), is interpreted as an isotropic size effect that gives a value D_{app}≈121 nm. If we consider that the shape of the coherence domains is spherical the corresponding diameter is $D=4/3D_{app}$≈161 nm. Attempts to refine an isotropic strain parameter (U) give nearly a zero value oscillating time to time to negative values. This value has consequently been fixed to zero. This means that with the present resolution of the instrument we cannot determine the presence of micro-strains in the A1 (HIP) sample.

We have two diffraction patterns of sample A2 corresponding to two orientations (A2 and A2'). The grain contributing to the diffraction patterns are not the same, so different values can be obtained for the refined parameters for this highly textured sample. The sample A2 gives also peaks more Lorentzian than those of the instrument, but it has also an additional isotropic Gaussian component due to strains.

For A2 the value of Y is higher than that of sample A1: Y= 0.055(2). This corresponds to a value D_{app}≈90.6 nm. If we consider that the shape of the coherence domains is spherical the corresponding diameter is

$D=4/3D_{app}\approx121$ nm. The additional U-parameters has a value U= 0.0175(15), this gives rise to an isotropic strain of $e=6.1x10^{-4}$.

For A2' the value of Y is significantly higher than that of sample A1: Y= 0.063(1). This corresponds to a value $D_{app}\approx78.6$ nm. If we consider that the shape of the coherence domains is spherical the corresponding diameter is $D=4/3D_{app}\approx105$ nm. The additional U-parameters has a value U= 0.013(1), this gives rise to an isotropic strain of $e=5.3x10^{-4}$.

Table V: Micro-structural information of samples A1 (ODS-304-HIP steel), A2 (A2') (ODS-304-HIP+F) and A3 (ODS-304-powder) obtained from the respective MIC files. See explanations in Table III

(A1)

h	k	l	2θ°	s=1/d(Å^{-1})	HGo(°)	HGi(°)	HLo(°)	HLi(°)	beta_TCH	App-Size(Å)
1	1	1	38.22	0.4823	0.4185	0.4185	0.0596	0.0162	0.8279	1208.02
2	0	0	44.43	0.5569	0.4033	0.4033	0.0633	0.0191	0.8279	1208.02
2	2	0	64.64	0.7876	0.3552	0.3552	0.0780	0.0295	0.8279	1208.02
3	1	1	77.66	0.9235	0.3284	0.3284	0.0902	0.0375	0.8279	1208.02
2	2	2	81.82	0.9646	0.3213	0.3213	0.0947	0.0404	0.8279	1208.02
4	0	0	98.26	1.1138	0.3101	0.3101	0.1166	0.0539	0.8279	1208.02
3	3	1	110.98	1.2137	0.3368	0.3368	0.1402	0.0679	0.8279	1208.02
4	2	0	115.44	1.2452	0.3586	0.3586	0.1506	0.0738	0.8279	1208.02
4	2	2	135.68	1.3641	0.5951	0.5951	0.2233	0.1146	0.8279	1208.02

(A2)

h	k	l	2θ°	s=1/d(Å^{-1})	HGo(°)	HGi(°)	HLo(°)	HLi(°)	beta_TCH	App-Size(Å)	strain(10^{-4})
1	1	1	38.21	0.4821	0.4211	0.4186	0.0740	0.0162	1.4318	906.49	6.1423
2	0	0	44.41	0.5567	0.4069	0.4033	0.0781	0.0190	1.5105	906.49	6.1423
2	2	0	64.62	0.7872	0.3650	0.3553	0.0942	0.0295	1.7658	906.49	6.1423
3	1	1	77.62	0.9231	0.3452	0.3284	0.1076	0.0375	1.9214	906.49	6.1423
2	2	2	81.78	0.9642	0.3412	0.3214	0.1127	0.0404	1.9689	906.49	6.1423
4	0	0	98.20	1.1133	0.3456	0.3100	0.1373	0.0539	2.1431	906.49	6.1423
3	3	1	110.91	1.2132	0.3875	0.3365	0.1641	0.0678	2.2609	906.49	6.1423
4	2	0	115.37	1.2447	0.4147	0.3582	0.1760	0.0737	2.2982	906.49	6.1423
4	2	2	135.57	1.3636	0.6756	0.5929	0.2588	0.1142	2.4394	906.49	6.1423

(A2')

h	k	l	2θ°	s=1/d(Å^{-1})	HGo(°)	HGi(°)	HLo(°)	HLi(°)	beta_TCH	App-Size(Å)	strain(10^{-4})
1	1	1	38.20	0.4820	0.4204	0.4186	0.0829	0.0162	1.5118	785.80	5.2968
2	0	0	44.40	0.5566	0.4060	0.4033	0.0871	0.0190	1.5743	785.80	5.2968
2	2	0	64.60	0.7871	0.3626	0.3553	0.1041	0.0295	1.7822	785.80	5.2968
3	1	1	77.60	0.9230	0.3410	0.3285	0.1184	0.0375	1.9111	785.80	5.2968
2	2	2	81.76	0.9640	0.3363	0.3214	0.1237	0.0404	1.9507	785.80	5.2968
4	0	0	98.18	1.1131	0.3368	0.3100	0.1501	0.0538	2.0963	785.80	5.2968
3	3	1	110.88	1.2130	0.3750	0.3364	0.1788	0.0677	2.1952	785.80	5.2968
4	2	0	115.33	1.2445	0.4008	0.3580	0.1915	0.0737	2.2266	785.80	5.2968
4	2	2	135.52	1.3633	0.6543	0.5919	0.2806	0.1141	2.3456	785.80	5.2968

(A3)

h	k	l	2θ°	s=1/d(Å^{-1})	HGo(°)	HGi(°)	HLo(°)	HLi(°)	beta_TCH	strain(10^{-4})
1	1	0	39.03	0.4920	0.4511	0.4165	0.2732	0.0165	6.0584	61.1415
2	0	0	56.38	0.6958	0.5238	0.3744	0.6212	0.0250	12.7950	91.4375
2	1	1	70.70	0.8522	0.4869	0.3420	0.5469	0.0331	10.4935	61.1415
2	2	0	83.84	0.9841	0.5419	0.3184	0.6923	0.0419	12.1169	61.1415
3	1	0	96.66	1.1002	0.7625	0.3095	1.1651	0.0524	18.1131	81.8395
2	2	2	109.82	1.2052	0.6631	0.3324	0.8290	0.0664	11.3764	46.8153
3	2	1	124.22	1.3018	1.0174	0.4283	1.4566	0.0881	16.0291	61.1415
4	0	0	141.77	1.3917	2.1052	0.7375	3.3446	0.1346	25.5901	91.4375

It is to be noticed that the sample A2 has significantly smaller coherence domains than those of sample A1. Moreover, the possibility to refine the U-parameter indicates that this sample has a micro-strain that is not negligible with respect to A1.

The micro-structural parameters of the powder sample are similar to those of the previous treated sample (B2), but in this case the anisotropy is more important.

The powder sample A3, shows a micro-structure characterised by the presence of strong anisotropic micro-strains, due to the presence of a high density of dislocations. The refined broadening of the peaks (through the parameters S_{400} and S_{220}), obtained from the automatically generated microstructure file, is shown in Table V. It is worth to notice that the integral breadth is an order of magnitude higher than the integral breadth of the ingot samples (A1, A2 and A2').

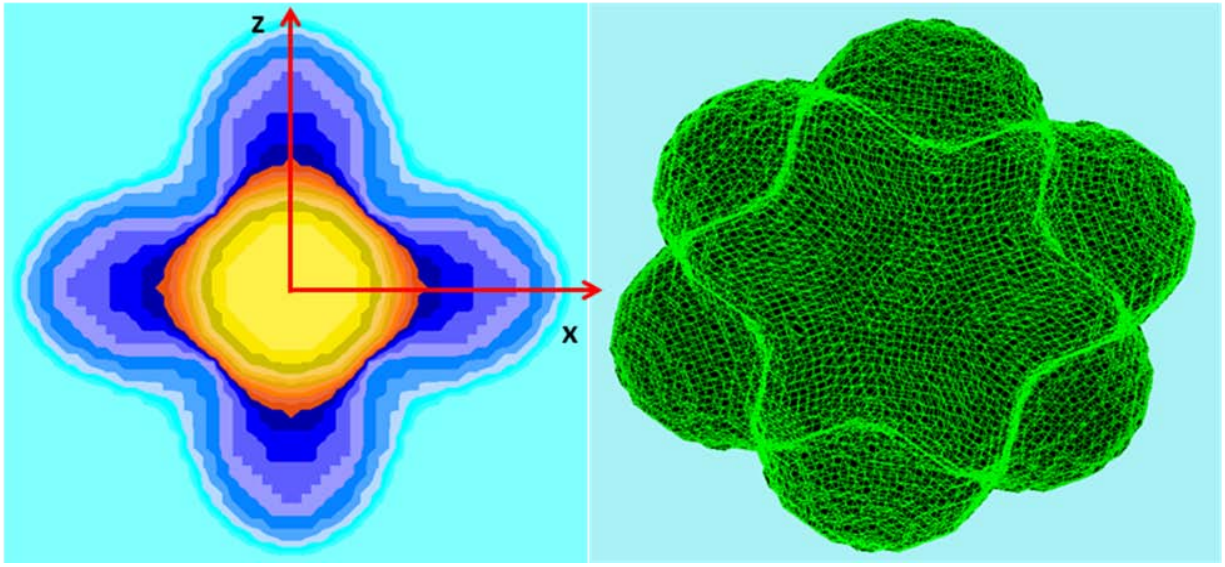

Figure 15: Micro-strain pattern of sample A3 (ODS-304-powder). On the left a projection of the strain surface is represented on the x-y plane. On the right a pseudo-3D representation of the strain surface is shown with a point of view along nearly [111]. The surface is similar to that of the sample B2, but the anisotropy is stronger.

In Figure 15 we show the strain surface for the sample A3, showing a similar aspect to that of Figure 6.

Treatment of the HXN-950 samples

The samples C1 (HXN-950, 1150°C), C2 (HXN-950, 1050°C) and C3 (HXN-950, 950°C) are nearly identical. We have refined using the Rietveld method the three diffraction patterns and we have obtained the results gathered in Table VI. The cell parameters are the same within two standard deviations and the isotropic temperature factor (Debye-Waller displacement parameter) diminish with increasing the temperature of the annealing treatment. This is normal because this parameter reflects not only the thermal vibrations but the degree of disorder and a part of the defect structure of the sample. By increasing the temperature of the annealing treatment it is expected that the intrinsic disorder of the alloys decreases in some way. The micro-structural parameters (in this case only Lorentzian components of size and strain) behave a little bit strangely. It seems that the micro-strain is higher for the samples with higher temperature treatment. This result should be regarded with caution because the values are very small and close to the limit of the resolution of the instrument

Table VI: Structural and micro-structural information of samples HXN-950 (annealed powder).

	C1-1150°C	C2-1050°C	C3-950°C
Cell parameter(Å)	2.87307(13)	2.87335(15)	2.87326(13)
B-iso(Å^2)	0.449(8)	0.467(8)	0.508(9)
X (isotropic Lorentzian strain)	0.128(4)	0.132(4)	0.020(4)
Y (isotropic Lorentzian size)	0.004(2)	0.036(3)	0.040(3)
Strain (x 10^{-4})	8.8	9.1	1.4
Apparent size (nm)	1191	138	123

On the other hand the size of the coherent domains follows the expected trend: an increase of the coherence length as the temperature of the heat treatment increases. The value of the apparent size of the sample C1 should be regarded with caution because it is in the limit of the experimental resolution. Within two standard deviations the size of the coherent domains may be considered as infinite as seen with the conditions of D20.

PART 2

Minor phases present in the samples

The possible minor phases present in the samples may be: carbides ($M_{23}C_6$, Fcc, cell 10.57-10.68 (Fe-Cr-Mo)$_{23}C_6$) or nitrides (TiN) or even totally unknown phases that have precipitated in the matrix. We can also explore the presence of other kind of phases (Y_2O_3, etc).

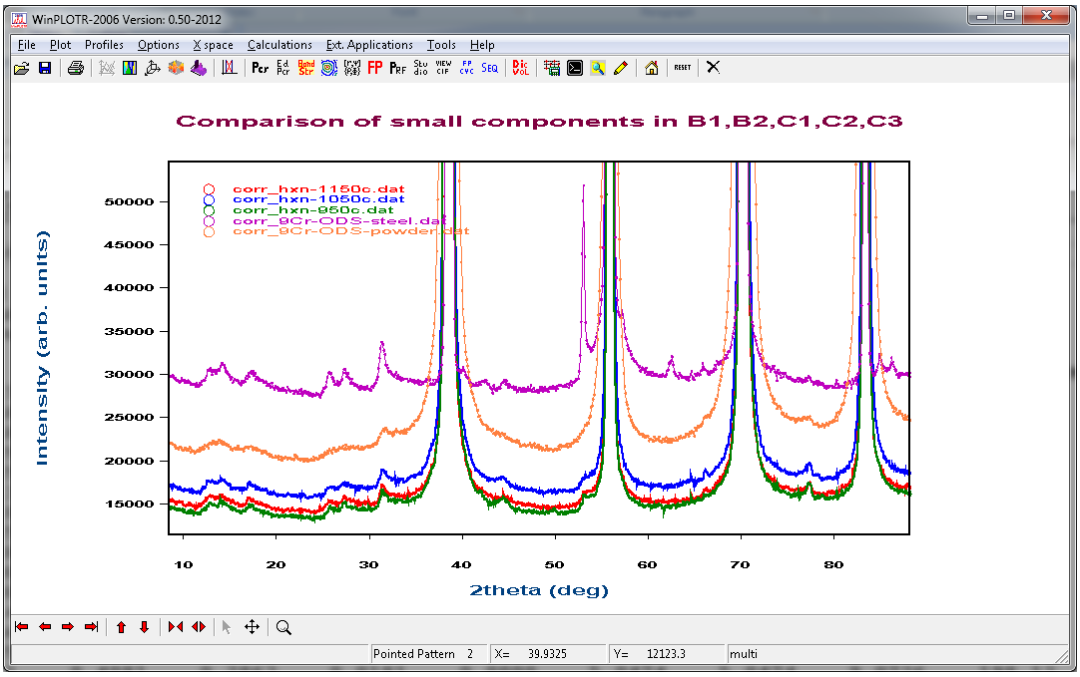

Figure 16: Comparison of samples B1-B2 (ODS-9Cr) with samples C1-C3 (HXN-950, HXN-1050, HXN-1150). It is important to realise that the minor phases seem to be the same in all these cases. In the steel sample (magenta) the peaks at 2θ=53.1 and 2θ=62.5 are more visible probably due to favourable texture.

The following series of figures represent the results of searching for the presence of known phases in the observed diffraction pattern.

In Figure 16 we show the low angle part of the diffraction patterns of the 9Cr-ODS and HXN samples. It is clear that all the samples share the same minor phases with different degrees of crystalline order. It is clearly seen the broader peaks in the 9Cr-ODS powder sample compared to the corresponding ingot.
The HXN samples (all of the same composition but with different heat treatments) present nearly identical characteristic minor phases.

If we compare the diffraction patterns of the samples A1 (ODS-304 HIP, steel) and B1 (ODS-9Cr, steel), other than the main peaks corresponding to ferritic (B1) and austenitic (A1) structures, we see some differences (Figure 17) clearly due to the fact that they have different compositions. However there are some features in the minor components that are common to both diffraction patterns.

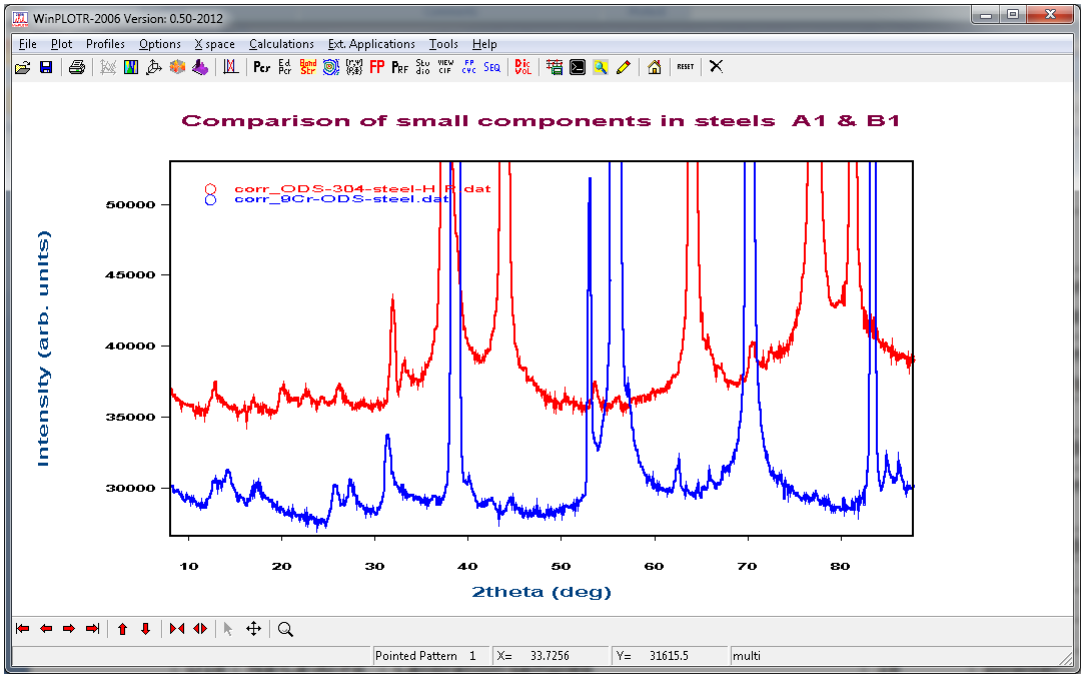

Figure 17: Comparison of samples A1 (ODS-304 HIP, steel) and B1 (ODS-9Cr, steel). It is important to realise at least some of the minor phases are present in both samples, however differences are clearly seen.

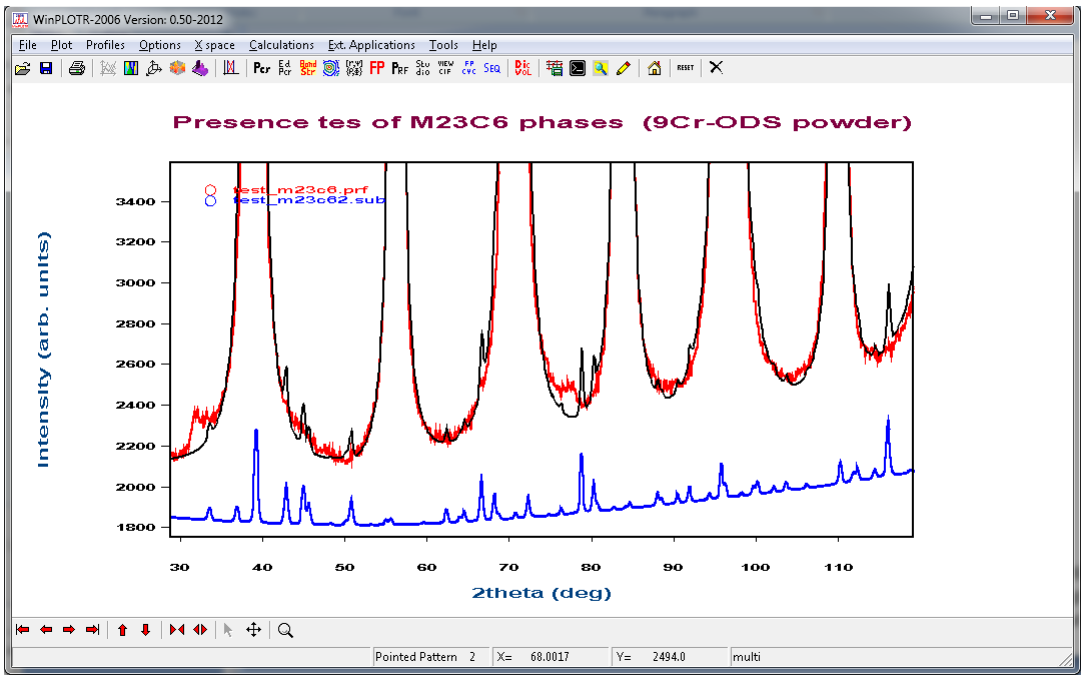

Figure 18: Presence test of $M_{23}C_6$ phases. The calculation is done by putting 0.51% of $Fe_{23}C_6$ (space group Fm3m, a=10.467 Å) and 99 nm apparent size. Notice that the calculate peaks are not visible in the experimental diffraction pattern.

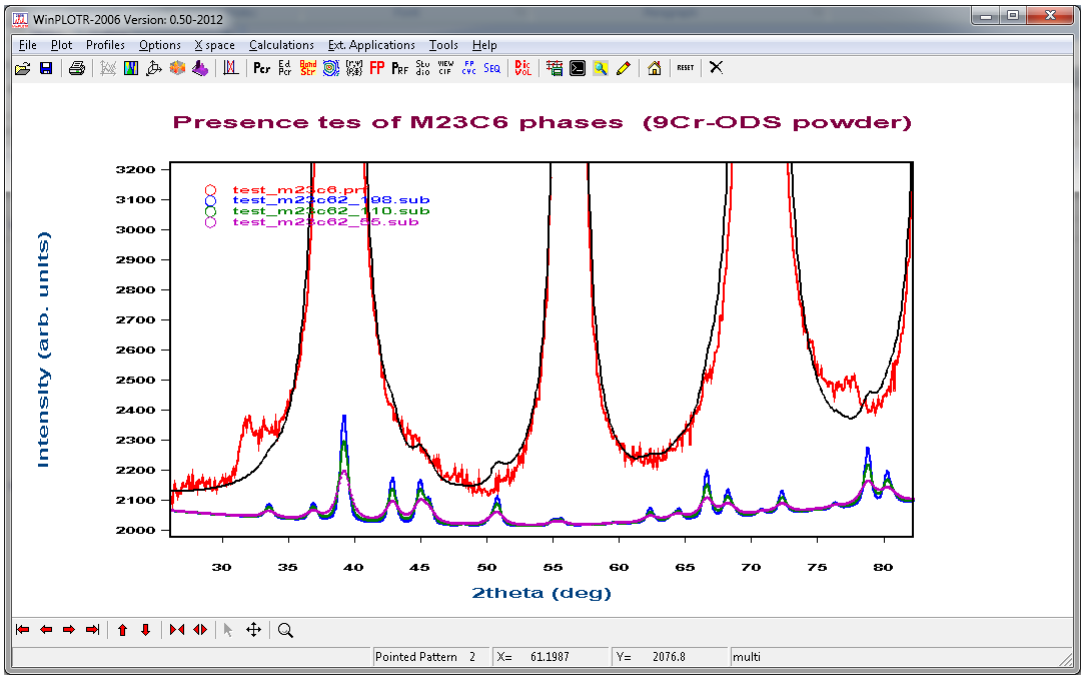

Figure 19: Presence test of $M_{23}C_6$ phases. The calculation is done by putting 0.51% of $Fe_{23}C_6$ (space group Fm3m, a=10.467 Å) and 5.5 nm apparent size. The contribution of the $Fe_{23}C_6$ is also given for 19.8 nm (blue) and 11.0 nm (green). Notice that the calculate peaks, for 5.5 nm (magenta), are not visible in the experimental diffraction pattern.

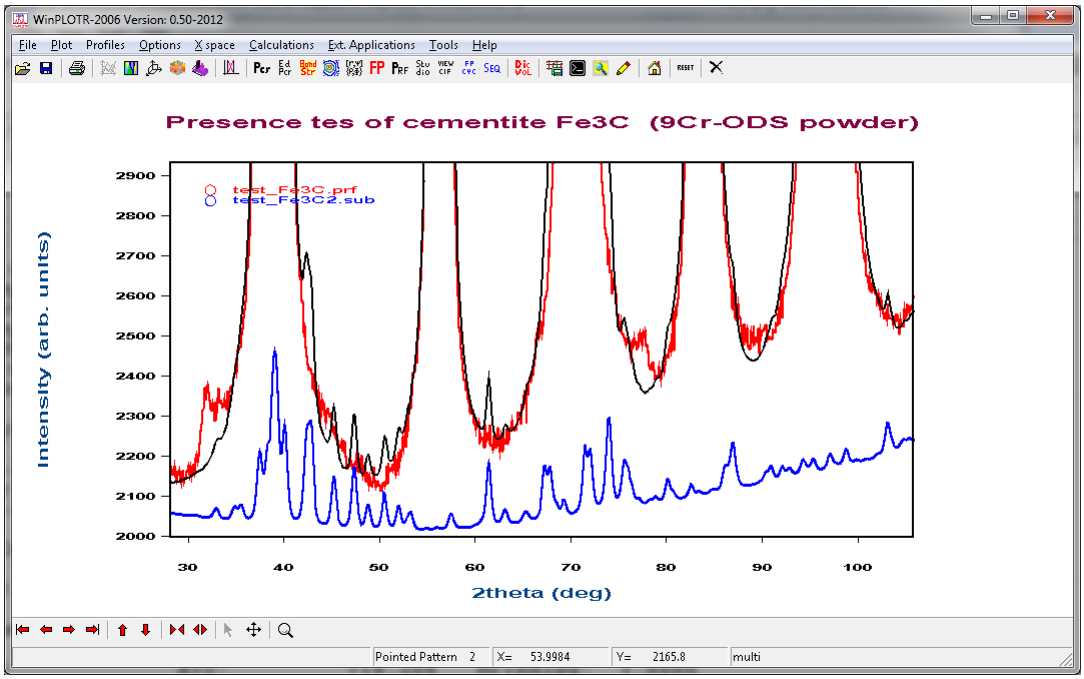

Figure 20: Presence test of cementite Fe_3C. The calculation is done by putting 1.25% of Fe_3C (space group Pnma, a= 5.084 Å, b= 6.745 Å, c= 4.514 Å,) and 20 nm apparent size. Notice that the calculate peaks are not visible in the experimental diffraction pattern.

We have tested the presence of the following phases: $M_{23}C_6$, M_3C, Y_2O_3 and TiN. For doing that we have added these phases into the input files of the already refined average structures.

The scale factor has been adjusted to provide a fraction of the minor phase that corresponds to some reasonable small amount in weight. We have used a microstructure corresponding to small coherence domains in order to explore the effect of broadening in the visibility of the final calculated pattern. Finally, we performed the calculation and compared visually with the observed diffraction patterns.

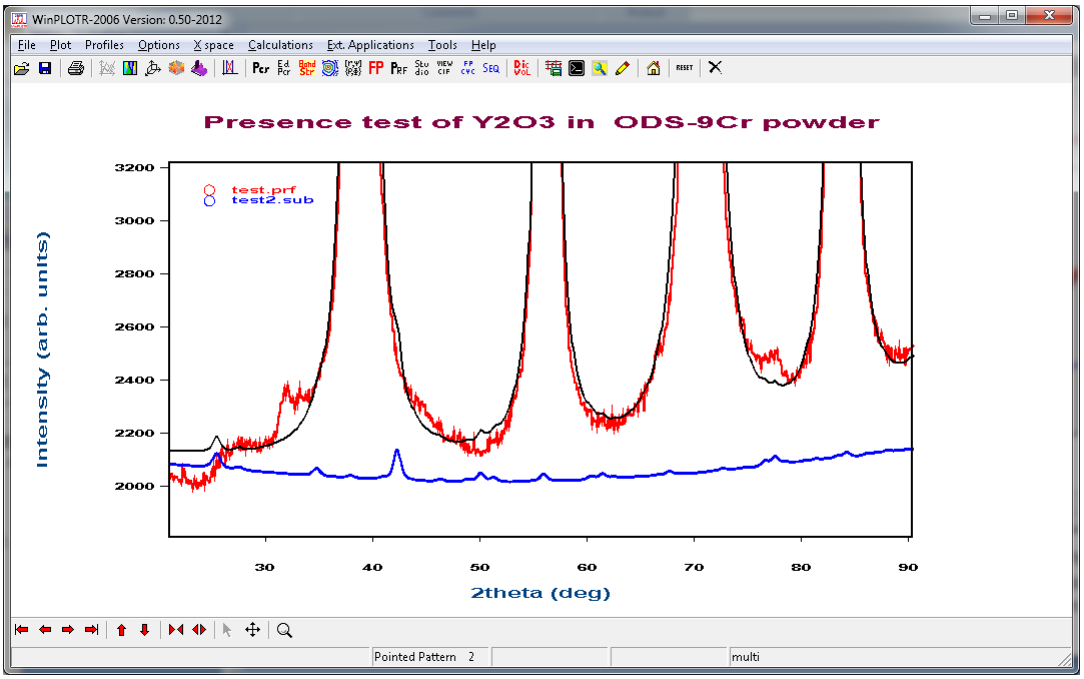

Figure 21: Presence test of Y_2O_3. The calculation is done by putting 0.35% of Y_2O_3 (space group I a 3, a= 5.084 Å) and 10 nm apparent size. Notice that the calculate peaks are not visible in the experimental diffraction pattern.

For the case of the ODS-304 powder, we have tested and refined the amount of a phase of TiNi-type (Fm3m), just to determine the limit of detection of this kind of phase. In Figure 22 we have represented the result of such a refinement together with the contribution of the TiN phase. We have refined the scale factor, the cell parameter, a= 4.203(9) Å and the Lorentzian size coefficient Y= 1.9(9). This gives rise to a tiny value of the apparent size (D_{app}=2.5(1.1) nm) which is clearly at the limit of the technique. The weight amount obtained from the refinement of the scale factor is x_{TiN}=0.25(9) %.

Notice that in Figure 22 the first small is not totally due to TiN. We can force the FWHM of the peak to a sharper value. This can be done by fixing the size parameter Y to a value giving a sharper peak, for instance Y=0.5, but in this case the refinement is worse because the other peaks in the pattern, in particular the peak (331) at 2θ=89.45 which is not overlapped to the peaks of the major phases, will rise above the background and this is not observed in the experimental diffraction pattern. At the same time the amount of the phase diminish up to 0.09%.

We have to say that if these phases exist within the samples they are present at a level well below the percentages in weight used for the calculations and provided in the caption of the figures.

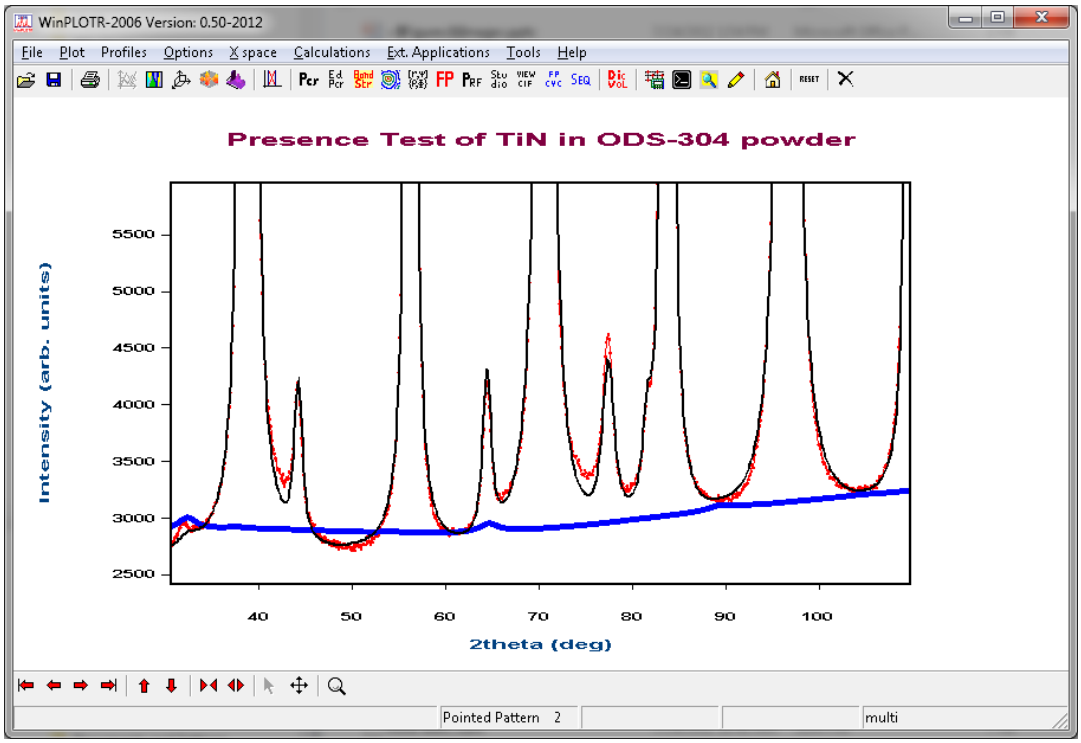

Figure 22: Presence test of TiN in ODS-304 powder. This is a real refinement leaving free the scale factor, the cell parameter and the Lorentzian size coefficient (see text). Notice that the first small peak is not totally due to TiNi.

Conclusions

We have analysed a series of samples and we have fully characterised (structural and micro-structural diffraction analysis) the major phase appearing in them. Clearly the powder samples present a strong anisotropic broadening (except those treated a high temperature like the HXN-950 samples) due to the presence of a high concentration of dislocations.

We have not been successful in determining the origin of the broad and asymmetric peaks existing in the low angle part of all the diffraction patterns. They must correspond to precipitates of unknown structure. A systematic study using electron diffraction and microscopy would be of interest in order to determine, at least, the unit cell of these precipitates. This may be difficult because the amount of phase is probably well below 1%. On the other hand, the asymmetric Warren-like peak shape may indicate a planar disordered structure of some precipitates. This is an indication that the unknown phases should appear in the grain boundaries and have a short correlation length in one single direction.

Allegato 2

Pubblicazione scientifica - R. Coppola , M. Klimenkov, R. Lindau, A. Möslang, M. Valli, A. Wiedenmann, J. N. Mat. 409 (2011) 100 -105

Journal of Nuclear Materials 409 (2011) 100–105

Contents lists available at ScienceDirect

Journal of Nuclear Materials

journal homepage: www.elsevier.com/locate/jnucmat

Recent applications of small-angle neutron scattering in the characterization of irradiated steels for nuclear technologies

R. Coppola [a,*], M. Klimenkov [b], R. Lindau [b], A. Möslang [b], M. Valli [c], A. Wiedenmann [d]

[a] ENEA-Casaccia, UTFISSM-PRONOC, Via Anguillarese 301, 00123 Roma, Italy
[b] Karlsruhe Institute of Technology, IMF I, PO Box 3640, D-76021 Karlsruhe, Germany
[c] ENEA-Faenza, UTTMATF, Via Ravegnana 186, 48018 Faenza, Italy
[d] Institut Max von Laue – Paul Langevin, 6 rue Jules Horowitz, 38042 Grenoble, France

ARTICLE INFO

Article history:
Available online 21 September 2010

ABSTRACT

Small-angle neutron scattering (SANS) is a powerful experimental tool to investigate the microstructural evolution under irradiation in steels for fission and future fusion reactor systems. We present recent SANS results concerning the modelling of helium bubble growth in F82H-mod. steel implanted with α-particles and the dose dependence of microstructural radiation damage in Eurofer-97 steel for fusion reactors irradiated at 250 °C. The discussion of these results is focussed on the quality of the metallurgical information obtained by such SANS measurements and consequently on their usefulness also for engineering and design purposes.

1. Introduction

Small-angle neutron scattering (SANS) is since long time assessed as a powerful experimental tool to investigate the microstructural evolution under irradiation in steels for fission and future fusion reactor systems. Reviews of experimental work carried out in this area can be found in Refs. [1–3]. SANS allows in fact to non-destructively investigate massive samples, to distinguish non-magnetic and magnetic defects (such as some kind of precipitates), to detect light elements, including hydrogen. Furthermore, combined with other techniques such as transmission electron microscopy (TEM), SANS measurements can provide fundamental information to experimentally check theoretical models. For a proper utilization of the results obtained by SANS measurements on complex steels, especially under irradiation, a good metallurgical characterization of the investigated material and complementary information by other techniques are necessary, especially if a quantitative characterization of metallurgical parameters such as volume fraction or average defect radius is required. This contribution presents two examples of SANS application in the characterization of structural steels for nuclear technologies. The first series of results concerns a refined analysis of SANS data aiming to contribute in the modelling of helium bubble growth in F82H-mod. steel implanted with α-particles. The second example concerns the dose dependence of microstructural radiation damage in Eurofer-97 steel for fusion reactors neutron irradiated at low temperature and shows the importance of characterizing the microstructural evolution in the un-irradiated, thermally treated material. In the first case only one kind of irradiation effect is assumed to be present and the data interpretation is relatively straightforward. In the second case SANS provides a tool to contribute in identifying the defects present in the steel, in the absence of a more detailed metallurgical characterization by other techniques. The discussion of these results will focus on the quality of the metallurgical information obtained by such SANS measurements and consequently on their usefulness also for engineering and design purposes.

2. Experimental technique and data analysis

Reference is made to [1,4] for a general presentation of SANS and to previous work [5] for its application to the study of martensitic steels, respectively. The SANS measurements reported in this paper were carried out at the D11 and D22 instruments at the High Flux Reactor of Institut Max von Laue – Paul Langevin, Grenoble. In the case of F82H-mod. steel a wavelength of 6 Å and sample-to-detector distances of 2 m (at D11) and 8 m (at D22) were used. Combining these two measurements gave a Q interval (the modulus of the scattering vector being $Q = 4\pi \sin\theta/\lambda$, where 2θ is the full scattering angle) ranging from 0.007 to 0.05 $Å^{-1}$, which corresponds to particle sizes ranging from approximately 10 to 150 Å. In the case of the Eurofer-97 steel the SANS measurements were carried at the D22 instrument at sample-to-detector distances of 2.00 m and 12 m with a wavelength λ of 6 Å, with a wavelength resolution of 10% and collimation distances of 5.6 m and 11.2 m. These experimental conditions gave a Q interval ranging from 0.002 to 0.3 $Å^{-1}$, which corresponds to particle sizes

* Corresponding author. Tel.: +39 06 30484727; fax: +39 06 30484747.
E-mail address: roberto.coppola@enea.it (R. Coppola).

0022-3115/$ - see front matter © 2010 Elsevier B.V. All rights reserved.
doi:10.1016/j.jnucmat.2010.09.012

ranging from 10 to 500 Å approximately. Calibration to absolute SANS cross-section was obtained by measurement of water in a quartz cell; the data were treated by the ILL standard programs [6]. A horizontal magnetic field was applied perpendicular to the incoming neutron beam in order to fully align the magnetic moments in the martensitic steels samples. Thus only nuclear scattering occurs in the horizontal plane, while nuclear and magnetic scattering occur in the vertical one. The purely magnetic scattering is obtained as the difference between the vertical and horizontal SANS cross-sections. In fact, in the case of magnetic samples, the total SANS cross-section $d\Sigma(Q)/d\Omega$ (where Ω stands for the solid angle) can be written as the sum of two terms

$$d\Sigma(Q)/d\Omega = d\Sigma(Q)/d\Omega_{\mathrm{nucl}} + d\Sigma(Q)/d\Omega_{\mathrm{mag}} \sin^2 \alpha \quad (1)$$

where α is the azimutal angle on the detector plane. The ratio of the "vertical" to the "horizontal" SANS components:

$$R(Q) = \frac{d\Sigma(Q)/d\Omega_{\mathrm{nucl}} + d\Sigma(Q)/d\Omega_{\mathrm{mag}}}{d\Sigma(Q)/d\Omega_{\mathrm{nucl}}} = 1 + (\Delta\rho)^2_{\mathrm{mag}}/(\Delta\rho)^2_{\mathrm{nucl}} \quad (2)$$

(defined also as "A" by other authors) is related to the composition of the microstructural inhomogeneities and its dependence on Q implies that defects of different size or composition are present in the investigated sample, $(\Delta\rho)^2$ being the "contrast" or square difference in neutron scattering length density (nuclear and magnetic respectively) between the observed nuclear and magnetic inhomogeneities and the matrix.

The SANS nuclear and magnetic cross-sections can each one be written as

$$D\Sigma(Q)/d\Omega = (\Delta\rho)^2 \int_0^\infty dRN(R)V^2(R)|F(Q,R)|^2 \quad (3)$$

where $N(R)$ is the number per unit volume of centers with a typical size between R and $R + dR$, V their volume and $|F(Q,R)|^2$ their form factor and $(\Delta\rho)^2$ is the nuclear or magnetic "contrast". The volume distribution function is defined as:

$$D(R) = N(R)R^3 \quad (4)$$

N(R) was determined, by transformation of Eq. (3), using the method described by in [7] and more recently discussed in [5] where the influence of background subtraction and the reliability of information referring to inhomogeneities corresponding to Q-values outside the available experimental range are discussed. This code assumes that the size distribution function can be described by a set of cubic B-spline functions, with equispaced knots in log R scale. The number of splines is determined by the R-range where the size distribution is to be explored (always larger than the range where different sizes can be effectively resolved) and by the required degree of detail. The logarithmic representation of $N(R)$ is quite suited for the case of technical alloys where different kinds of microstructural inhomogeneities with sizes differing in order of magnitude may be simultaneously present. The positive nature of the size distribution function is added to the fitting procedure as the only *a priori* information. This assumption and other restrictions or constraints, such as the "regularization" employed to ensure convergence, do not affect the final result, which is the smoothest distribution that is compatible with the scattering data. The number of splines is determined by the required degree of accuracy and by the length of the R-range where the size distribution is to be explored; this is always larger than the range where different sizes can be effectively resolved. Number of splines, R-range and background parameter are optimized in order to find the minimum χ^2 value giving a physically meaningful $N(R)$. For each measurement the fitting procedure is repeated on many different scattering profiles obtained from the measured one by adding a random error with a standard deviation equal to the statistical error. The 80% confidence region of the size distributions is then plotted together with the size distribution corresponding to the best-fit of the measured spectrum. The upper and lower limits of this error band allow one to estimate the uncertainty associated to the volume fraction ΔV, while the uncertainty on the average radius R can be estimated as the full width at half maximum of the distribution, provided the maxima in $N(R)$ are symmetric enough.

3. Helium bubble growth in F82H-mod. steel

3.1. Material characterization

The chemical composition of F82H-mod. steel is: 8.0 Cr, 0.10 C, 0.16 Mn, 0.16 V, 2.0 W, 0.02 Ta Fe bal wt.%. 0.4 mm thick samples with a surface of approximately 1 cm^2 were homogeneously implanted at 250 °C with 400 appm (atomic part per million) He, using 104 MeV α-particles at the cyclotron facility of the FZK. They were then submitted to 2 h tempering (at 525 °C, 825 °C and 975 °C) in high vacuum, together with non-implanted samples of the same material (one for each temperature) serving as a reference to isolate the SANS signal arising from the helium bubbles. A sample of the same material tempered at 250 °C for a duration equivalent to the implantation time (approximately 5 days) served as a reference for an as-implanted sample (at 250 °C with 400 appm) and was not further thermally treated. It was assumed that the microstructural effect produced at 250 °C can be neglected in the high-temperature tempered samples. The definition and preparation of thermal reference samples is a critical issue in such complex steels, where a variety of phases may precipitate following different thermal treatments. Previous work carried out on un-irradiated F82H-mod. steel both by TEM and by SANS [8] has shown that, at temperatures around 550 °C, even slight changes in tempering or ageing temperature and time can result in significantly different microstructures. For example, increasing the tempering temperature from 525 °C to 550 °C gives an increase of almost one order of magnitude in the SANS cross-section due to the onset of fine M_2C precipitation at this temperature. On the other hand, above the re-austenitisation temperature (835 °C) changes in tempering temperature have little influence on the microstructure evolution, which is dominated by the growth of large $(Cr,Fe)_{23}C_6$ carbides. In all the investigated samples the TEM observations show clearly the presence of helium bubbles. An example of the specimen tempered at 975 °C is shown in Fig. 1. The helium bubbles are often situated along the lines which are marked by arrows in Fig. 1a. Possibly these are 1-dimensional defects, the former dislocations lines which disappear after heating over the austenitisation temperature. This can be confirmed by observation of bubbles agglomeration marked by circles in the other grain. In this case the dislocation lines were oriented perpendicular to the foil surface. Only 2–3 bubbles remain from the line after preparation of TEM foil. The corresponding histograms which demonstrate the change of size distribution with the irradiation temperature are shown in the next section compared with the neutron data.

3.2. SANS results and discussion

The SANS measurements were carried out at the instruments D11 [10,11] and D22 [12]. Ref. [12] reports the results of a preliminary analysis carried out on the two data sets; a further refinement of this analysis, presented here after, was carried out with the aim of improving its accuracy and contribute in the modelling of the growth mechanism. More specifically the helium concentration C_{He} was determined from the SANS data as [13]

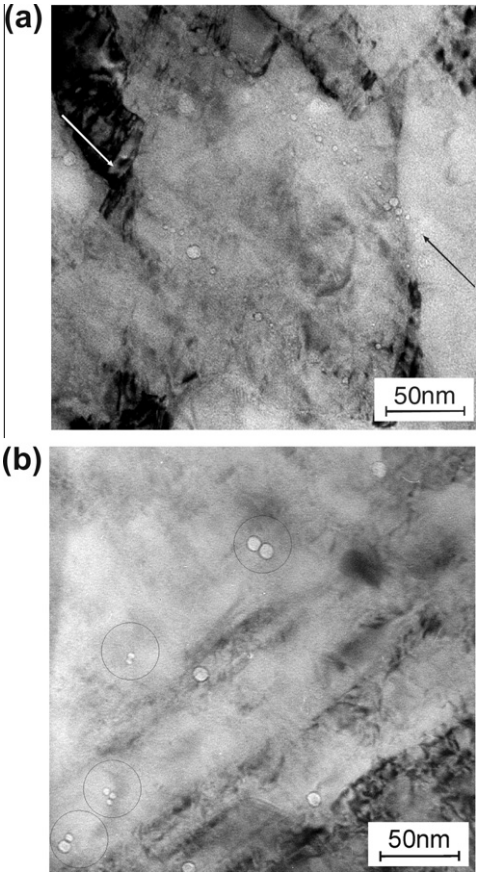

Fig. 1. TEM image of F82H-mod. steel implanted at 250 °C with 400 appm helium then tempered for 2 h at 975 °C. In the part (a) the bubbles are ordered along the marked lines. The pairs of helium bubbles are marked with a circles in the part (b) [9].

$$C_{He} = v_M \int \rho_{He}(R)V(R)N(R)dR \tag{5}$$

where $v_M = 0.5 \cdot 2.87\ \text{Å}^3$ is the F82H-mod. steel matrix atomic volume.

The dependence of the contrast on the bubble radius was taken into account following the fitting procedure reported in [14,15], although given the small value of $\rho_{He} = 0.588 \cdot 10^{10}\ \text{cm}^{-2}$ [3], very large changes of the helium mass density would be necessary to lead to significantly different distributions. Assuming that the helium concentration is equal to the nominal value (400 appm), the obtained variations on $(\Delta\rho(R))^2$ range typically from −10% at 2 Å to +12% at 100 Å. The resulting variations in $N(R)$ are generally of a few per cent, therefore well inside the statistical uncertainty band determined in previous work [10,11] where it had been assumed that $(\Delta\rho)^2 = (\rho_{He} - \rho_{F82H})^2 = 4.833 \cdot 10^{21}\ \text{cm}^{-4}$ [3]. The variable contrast function determined in this way has been included in the iterative procedure described in Section 2 to determine the distributions but without unphysical oscillations (which can be produced by an excessive number of splines). A constant background was introduced as an additional parameter in order to take into account the uncertainties relating to the subtraction of the reference sample [11,12]. Since the helium bubbles are non-magnetic inhomogeneities imbedded in a fully magnetized martensitic matrix, the nuclear and magnetic SANS components are identical and $R(Q) = 2$ within the experimental uncertainties. Fig. 2 shows the differences between implanted and reference samples. At 525 °C this difference is smaller than the experimental errors. This has been tentatively attributed to the slight differences in the thermal history of the two samples and to precipitation of the M_2C phase around this temperature [8,10]. The fact that no significant difference is observed by TEM between the as-implanted sample and the one tempered at 525 °C after implantation further supports this interpretation. It is also noted that previous SANS experiments carried out on a similar steel implanted with much higher helium (1200 appm) detected no difference between implanted and reference samples for tempering around this same temperature [13]. The best-fit $D(R)$ distributions at 250 °C, 825 °C and 975 °C are shown in Figs. 3a–5a, while Figs. 3b–5b show the comparison of the SANS data with the corresponding TEM histograms in the overlap region. The $D(R)$ distribution is considered for these

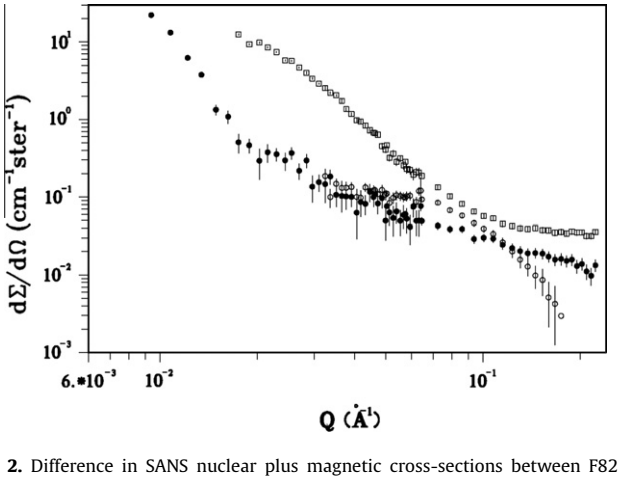

Fig. 2. Difference in SANS nuclear plus magnetic cross-sections between F82 h-mod. steel implanted and reference samples: as-implanted at 250 °C (empty dots), after tempering at 825 °C (full dots), after tempering at 975 °C squares).

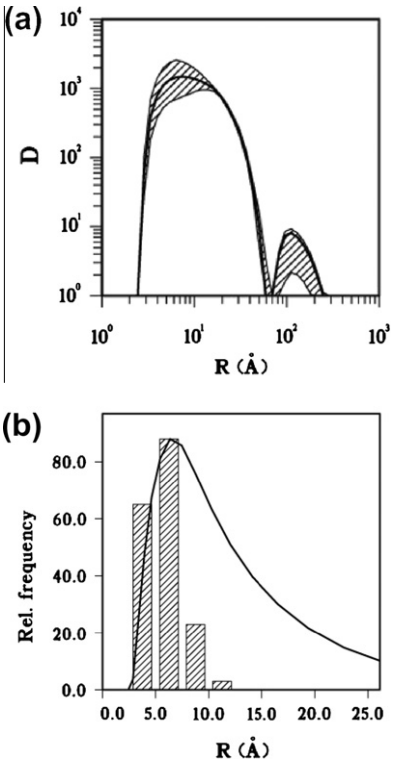

Fig. 3. (a) Best-fit He bubble volume distributions $D(R)$ in Å^{-1} in F82H-mod. steel as-implanted at 250 °C. The dashed area represents the 80% confidence band. (b) Comparison with the corresponding TEM histogram the relative intensities of SANS and TEM data, in arbitrary units, are normalized by their respective maxima.

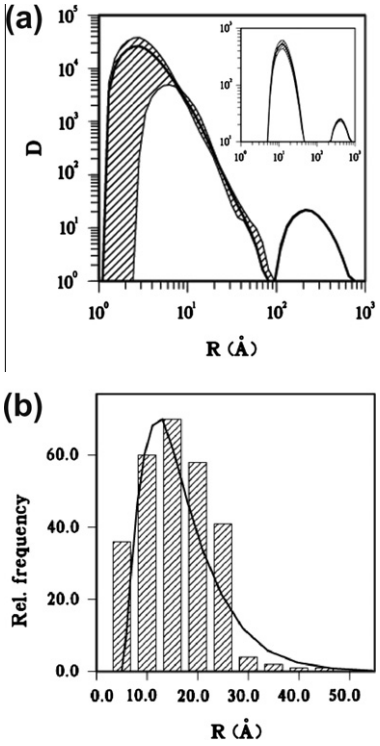

Fig. 4. (a) Best-fit He bubble volume distributions $D(R)$ in Å^{-1} in F82H-mod. steel as-implanted at 250 °C then tempered at 825 °C. The dashed area represents the 80% confidence band; the inset in the upper right corner shows the distribution fitting the TEM histogram, which is obtained by increasing the background parameter from 0.001 cm^{-1} to 0.012 cm^{-1}. (b) Comparison with the corresponding TEM histogram in the overlap region: the relative intensities of SANS and TEM data, in arbitrary units, are normalized by their respective maxima.

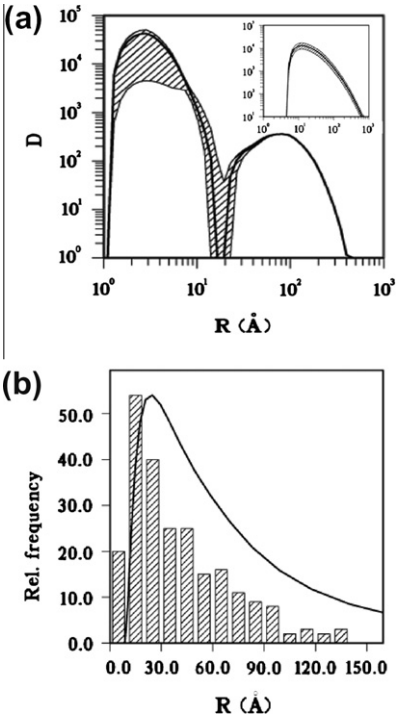

Fig. 5. (a) Best-fit He bubble volume distributions $D(R)$ in Å^{-1} in F82H-mod. steel as-implanted at 250 °C then tempered at 975 °C. The dashed area represents the 80% confidence band; the inset in the upper right corner shows the distribution fitting the TEM histogram which is obtained by increasing the background parameter from 0.0022 cm^{-1} to 0.059 cm^{-1}. (b) Comparison with the corresponding TEM histogram in the overlap region: (the relative intensities of SANS and TEM data, in arbitrary units, are normalized by their respective maxima).

comparisons since for the reasons explained in Section 2 the TEM observations, which are limited to sizes larger than 10 Å, give a higher statistical weight to the larger bubbles. Furthermore, the SANS cross-section increases with R^6 (Eq. (2)). Table 1 lists the best-fit helium bubble volume fraction and helium concentration values, together with the bubble radii averaged over the $D(R)$ and the $N(R)$ distributions (R_V and R_N, respectively).

The weighted average radii and volume fractions values obtained by TEM are reported as well. The errors on the R and ΔV values obtained by SANS are approximately 30%. However, since they are determined by the extremes of the uncertainty band, they can be as large as 50% where this band is larger, for $R < 10$ Å, and considerably smaller for high R values. These new results (Figs. 3a,4a,5a) are in good agreement with the distributions determined in the previous experiment [10,11], where a more limited Q-range was available. Extending the measurements to small Q's results in a smaller uncertainty band, especially for $R > 100$ Å, and in a more accurate representation of the whole distribution. After implantation at 250 °C the bubbles are quite small and homogeneously distributed in size (Fig. 3a). The best-fit SANS distribution is in good agreement with TEM (Fig. 3b) and no background correction is needed. Also the average radius and volume fraction values determined by the two techniques are in agreement (Table 1). The C_{He} value determined by SANS is significantly lower than the nominal one, suggesting that only part of the implanted helium has given rise to detectable bubbles.

After tempering at 825 °C the helium bubbles increase in size and volume fraction with a corresponding broadening of the distribution (Fig. 4a). The best-fit SANS distribution shows a high density of bubbles with sizes below the resolution limit of TEM.. There is also an indication of bubbles as large as 200–300 Å, with a two orders of magnitudes lower peak intensity. The best-fit volume fraction value determined by SANS still agrees with the corresponding TEM value within the experimental uncertainties, but increases significantly with respect to the as-implanted sample. The helium concentration value determined by the SANS measurements is in good agreement with the nominal one. A direct comparison with the TEM histogram requires in this case an increase of the background parameter from 0.001 cm^{-1} (best-fit distribution of Fig. 4a) to 0.012 cm^{-1}: this means suppressing from the corresponding SANS spectrum of Fig. 4 the data for $Q > 0.160$ Å^{-1}, which in real space corresponds precisely to the size range below the resolution limit of TEM. Such a background subtraction results in the distribution of the inset in Fig. 4a, which is compared with the TEM histogram in Fig. 4b. In the SANS–TEM overlap region ($R > 10$ Å) the average radii determined by the two techniques agree too (both considering R_V and R_N). The best-fit distribution at 975 °C (Fig. 5a) shows a further increase in the density both of bubbles smaller than 10 Å and of the one order of magnitude larger bubbles. The best-fit volume fraction is significantly higher than the corresponding TEM value, while the C_{He} value is higher than

Table 1
Best-fit He bubble volume fraction, ΔV, He concentration, C_{He}, and radii averaged over the $D(R)$ and the $N(R)$ distributions (R_V and R_N respectively) obtained from SANS data; at 825 °C and 975 °C the R_V values in italics are averaged to the portion of the $D(R)$ compared with the TEM histograms in the insets of Figs. 4a and 5a. The R and ΔV values in parentheses are those obtained from TEM.

Tempering temperature (°C)	ΔV	C_{He} (appm)	R_V (Å)	R_N (Å)
250	0.0012 (0.0039)	209.0	11.1 (7)	6.2
825	0.0053 (0.0036)	375.9	3.8 14.6 (17)	10.5
975	0.0085 (0.0054)	558.9	4.1 45.9 (46)	15.3

the nominal one but compatible with it within the experimental uncertainties. Also in this case a direct comparison with the TEM histogram requires an increase of the background parameter from 0.022 cm^{-1} (best-fit distribution of Fig. 5a) to 0.059 cm^{-1}: this means suppressing from the corresponding SANS spectrum of Fig. 2 the data for $Q > 0.170$ $Å^{-1}$, which in real space corresponds precisely to the size range below the resolution limit of TEM. Such a background subtraction gives the distribution of inset in Fig. 5a, which is compared with the TEM histogram in Fig. 5b. It is therefore clear that for this high tempering temperature (which is expected to enhance the nucleation and growth processes) a discrepancy between the SANS and TEM results arises because a strong increase in the bubble distribution occurs for bubble sizes that are practically invisible by conventional TEM. In the overlap region the TEM and SANS average radii agree considering the R_V value, since the lower R_N value is clearly determined by the population of bubbles as small as 4 Å approximately. Finally, it is noted that the distribution in the inset of Fig. 5a yields a value of the volume fraction (0.0058) almost coincident with the TEM one.

The present results confirm and complete the previous findings on bubble growth in helium implanted F82H-mod. steel [10–12]. These results suggest that a homogeneous and narrow bubble distribution produced in the as-implanted material evolves by tempering, on a time scale as short as 2 h, into a population of much larger and stable helium bubbles, while the remaining helium atoms implanted in the matrix give rise to bubbles smaller than 10 Å (which are hardly visible by SANS and invisible by TEM).

4. Microstructural evolution under low-temperature neutron irradiation in Eurofer-97 steel

The Eurofer-97 sample (9 Cr, 1 W, 0.2 V, 0.1 C wt.%) was irradiated at 250 °C and 300 °C at the HFR-Petten up to target dose levels of 2.5, 8.4 and 16.5 dpa [16–20]. The results of SANS measurements carried out on 2.5 dpa and 8.4 dpa irradiated Eurofer are reported in Refs. [18,19]. was also measured. In a more recent SANS experiment [20] Eurofer-97 irradiated at 250 °C to 16.5 dpa was investigated by SANS together with an un-irradiated samples of the same Eurofer-97 heat, submitted to thermal treatment 1040 °C 30' + 760 °C 2 h; also the previously investigated Eurofer-97 sample irradiated at 300 °C to 8.4 dpa was measured in the same, wide Q-range, in order to obtain a more accurate characterization. The results are summarized in Figs. 6–8. Figs. 6 and 7 show the nuclear SANS components of the irradiated and reference Eurofer-97 samples respectively; for completeness the data referring to irradiation dose 2.4 dpa have been included [16]. Marked differences are

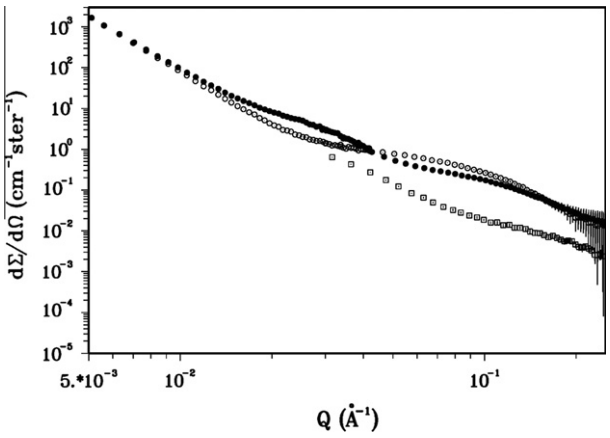

Fig. 6. Eurofer-97 irradiated at 250 °C 2.5 dpa (squares), at 300 °C 8.4 dpa (full circles) and at 250 °C 16. 3 dpa (empty circles).

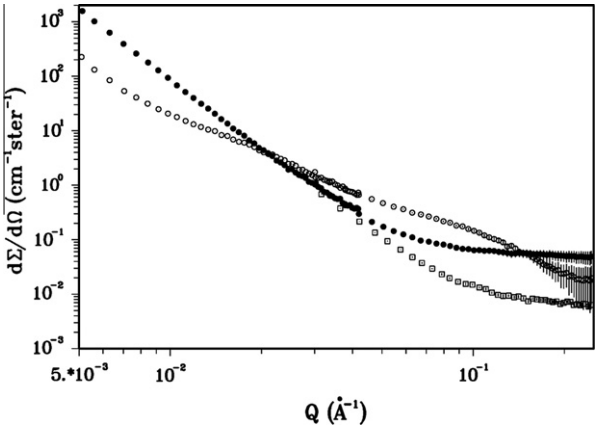

Fig. 7. Eurofer-97 un-irradiated references for irradiated at 250 °C 2.5 dpa (squares), at 300 °C 8.4 dpa (full circles) and at 250 °C 16. 3 dpa (empty circles).

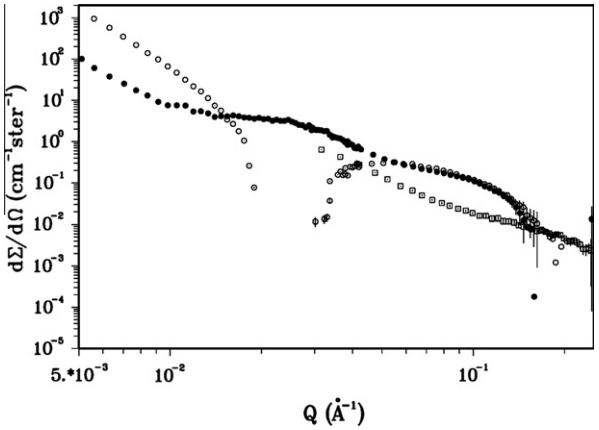

Fig. 8. Difference between the nuclear SANS components of irradiated Eurofer-97 and reference sample for irradiated at 250 °C 2.5 dpa (squares), at 300 °C 8.4 dpa (full circles) and at 250 °C 16. 3 dpa (empty circles).

detected among the un-irradiated reference samples, particularly between those referring to 8.4 and 16.5 dpa dose level: that is to be possibly attributed to the different duration of the irradiation and to the different irradiation temperatures (300 °C for 8.4 dpa and 250 °C for 16.5 dpa), which reflect in considerable microstructural changes. As a consequence, after subtraction of the un-irradiated samples from the irradiated ones (Fig. 3) it appears that increasing the irradiation dose from 8.4 to 16.5 dpa a consistent increase in the distribution of defects larger than 50 Å is observed; their corresponding $R(Q)$ value is approximately 3.5, therefore they cannot be identified as simple microvoids, but rather as Cr-rich precipitates such as α' ones [5,21]. For 8.4 and 2.5 the results are consistent with the previous ones [16,17] in the high-Q range, that is $R(Q)$ is close to two suggesting the presence of microvoids. However, for smaller Q-values its value suggests the presence of Cr-rich precipitates also at 8.4 dpa. The previous results [19] have shown that increasing the dose from 2.4 to 8.9 dpa the volume fraction of the microvoids increases by a factor of nearly 2 while their average size remains nearly unchanged. Increasing the dose to 16.5 seems to produce a completely different defect distribution, but a quantitative determination of such distribution requires to check by other techniques such as TEM the nature of the observed defects. Also the effect of thermal ageing at low temperatures (250–300 °C) for long ageing times has to be carefully investigated, since the microstructural effect of the irradiation is estimated by subtracting from the irradiated sample the thermal reference

samples; consequently uncertainties in the actual ageing conditions of the latter can introduce large errors in the final result and in the distributions obtained for the irradiated material. The data of Fig. 6 shows that increasing the irradiation dose from 8.4 to 16.5 dpa does not produce large microstructural effects in Eurofer-97 steel, which seems to confirm the good radiation resistance of this material. However Fig. 7 seems to suggest that the microstructure Eurofer-97 is quite sensitive to low-temperature ageing treatments, which must be kept into account for a more refined interpretation of the results form the irradiated material. In fact Fig. 8 shows that taking into account the behaviour of the reference samples increasing the dose to 16.5 changes completely the defect distribution and, possibly, their nature, since magnetic precipitates would prevail on microvoids. This tentative interpretation of the obtained results has to be carefully checked by TEM work and by additional SANS measurements on the un-irradiated material.

5. Conclusions

The two series of SANS results presented here above show once more how useful the information obtained by this technique can be to a metallurgical qualification of nuclear materials and of their microstructural evolution under irradiation. In the simple case of helium bubbles produced by implantation and tempering in F82H-mod. steel extending the experimental Q window improves the accuracy of the SANS measurements and the reliability of the metallurgical parameters their analysis provide. A realistic model of bubble growth is obtained in the explored irradiation and tempering conditions, with an estimate of the metallurgical parameters that is consistent with TEM results. However, in future SANS experiments the accuracy of similar results could be greatly improved by a more accurate evaluation of the background noise, which affects particularly the population of very small helium bubbles or clusters: to this end an accurate evaluation of the effects of low-temperature ageing is necessary. Work is also underway on this and other data sets to try and asses in a more general way the errors associated in the determination of the metallurgical parameters from the SANS data obtained in the case of very low defect volume fractions [22]. In the more complex case of low-temperature neutron irradiated Eurofer-97, the SANS measurements can provide for the moment only a preliminary and qualitative indication on the microstructural evolution, given also a lack of exhaustive observations of this steel by TEM and other microstructural techniques. However, extending the SANS measurements to a wide Q-range with respect to the previous ones [19] suggests that different kinds of irradiation defects can be simultaneously present with quite different sizes: small microvoids and large Cr-rich carbides. This would imply that modelling the irradiation behaviour of a this technical steel is a complex task, especially if higher doses and temperatures have to be considered. These SANS measurements also show that even slightly different low temperature treatments can give rise to consistent microstructural changes, which have to be carefully taken into account in the evaluation of the irradiation behaviour.

Acknowledgements

The ILL is gratefully acknowledged for valuable technical assistance in handling the irradiated material and running the SANS experiments; Dr. R.P. May is acknowledged for scientific discussions. Concerning the results reported in Section 4, this work, supported by the European Commission under the contract of Associations, was carried out within the framework of the European Fusion Development Agreement. The views and opinions expressed herein do not necessarily reflect those of the European Commission.

References

[1] Kostorz G, Neutron and X.ray Scattering Ch. 12 in Physical Metallurgy, R. W. Cahn, P. Haasen (Eds.) fourth Edition, 1996 pp 1115–1199.
[2] G. Albertini, R. Coppola, Nucl. Instrum. Methods A 314 (1992) 352.
[3] G. Albertini, R. Coppola, F. Rustichelli, Phys. Rep A 233 (3) (1993) 137.
[4] M.T. Hutchings, C.G. Windsor, Industrial Applications, in: K. Sköld, D.L. Price (Eds.), Methods of Experimental Physics, Neutron Scattering, vol. 23-c, Academic Press, 1987, pp. 405–482.
[5] R. Coppola, R. Kampmann, M. Magnani, P. Staron, Acta Mater. 46 (1998) 5447.
[6] R.E. Ghosh, S.U. Egelhaaf, A.R. Rennie, ILL report ILL98GH14T, 1998.
[7] M. Magnani, P. Puliti, M. Stefanon, Nucl. Instrum. Methods A 271 (1988) 611.
[8] R. Coppola, K. Ehrlich, M. Magnani, E. Materna-Morris, M. Valli, J. Nucl. Mater. 258–263 (1998) 1291–1294.
[9] M. Klimenkov, unpublished work.
[10] R. Coppola, M. Magnani, R.P. May, A. Möslang, J. Appl. Cryst. 33 (2000) 469.
[11] R. Coppola, M. Magnani, R.P. May, A. Möslang, M. Valli, J. Nucl. Mater. 283–287 (2000) 183.
[12] R. Coppola, M. Klimiankou, R. Lindau, A. Möslang, M. Valli, J. Nucl. Mater. 329–333 (2004) 1057.
[13] G. Albertini, F. Carsughi, R. Coppola, F. Rustichelli, D. Schwahn, G. Mercurio, Nucl Instrum. Methods A 321 (1992) 381–384.
[14] Li. Qiang, W. Kesternich, H. Schroeder, D. Schwahn, H. Ullmaier, Acta Metall. Mater. 38 (1990) 2383–2392.
[15] F. Carsughi, W. Kersternich, D. Schwahn, H. Ullmaier, H. Schroeder, J. Nucl. Mater. 191–194 (1992) 1284–1288.
[16] J. Rensman, R. Den Boef, F. P. van den Broek, E. D. L. van Essen, J. van Hoepen, J. Nucl. Mater., vol. 307–311, 2002.
[17] J. Rensman, NRG report 20023/05 68497/P, 2002.
[18] R. Coppola, R. Lindau, M. Magnani, R.P. May, A. Möslang, J.W. Rensman, B. van der Schaaf, M. Valli, Fract. Eng. Des. 75–79 (2005) 985.
[19] R. Coppola, R. Lindau, R.P. May, A. Möslang, M. Valli, J. Nucl. Mater. 386–388 (2009) 195–198.
[20] R. Coppola, Report for the fusion technology programme (TW6-TTMS001-D06), December 2009.
[21] E. Materna-Morris, A. Möslang, R. Rolli, H.-C. Schneider, J. Nucl. Mat. 386–388 (2009) 422–426.
[22] R. Coppola, F. Fiori, M. Valli, in preparation.

Allegato 3

Riassunto R. Coppola, M. Klimenkov, R. Lindau, L. Porcar, M. Valli, accettato per presentazione orale alla International Small-Angle Scattering Conference, sas2012, Sydney, November 2012

ACCETTATO PER PRESENTAZIONE ORALE ALLA INTERNATIONAL SMALL ANGLE SCATTERING CONFERENCE, SAS2012, SYDNEY, NOVEMBER 2012

OPTIMISATION OF SANS DATA ANALYSIS FOR MODELLING MICROSTRUCTURAL RADIATION DAMAGE IN NUCLEAR STEELS

***Coppola, R*[1]**, Klimenkov, M[2], Lindau, R[2], Porcar, L[3], Sepielli, M.[1], Valli, M.[4]

[1] *ENEA-Casaccia, Via Anguillarese 301, 00123 Roma, Italy*
[2] *KIT-IAM, PO Box 3640, D- 76021 Karlsruhe, Germany*
[3] *ILL, 6, rue Jules Horowitz, 38042 Grenoble, France*
[4] *ENEA- Faenza, Via Ravegnana 186, 48018 Faenza (RA), Italy*

SUMMARY

Combined with other microstructural techniques, such as electron microscopy and atom probe tomography, small-angle neutron scattering (SANS) provides a powerful experimental tool to quantitatively investigate the microstructural effects of radiation damage not only in model alloys but also in technical steels developed for advanced fission reactors and for the future fusion reactors. In fact, the analysis of the SANS data from irradiated steels provides relevant metallurgical parameters, such as irradiation defects volume fraction and average size, to be compared for experimental validation with the theoretical predictions, in order to contribute in the modelling of irradiation behavior under service conditions. To this end, an optimization of the SANS data analysis and an accurate evaluation of the associated uncertainties are essential.

This contribution will present original SANS data obtained, at the D22 instrument of the Institut Max von Laue - Paul Langevin in Grenoble, on neutron irradiated ferritic/martensitic steels developed for nuclear applications. Different transformation methods of the SANS data have been utilized and compared to assess the reliability of the size distribution functions for the irradiation defects (microvoids, helium bubbles) and to evaluate the resulting uncertainty. These results are compared with information available from other experimental techniques and from theory.